



JGR Solid Earth

RESEARCH ARTICLE

10.1029/2024JB029890

Key Points:

- Global age-depth ($n = 10,863$) and heat flow ($n = 3,573$) measurements are used to reassess different oceanic plate cooling models
- Simple and comprehensive parameterizations yield similar estimates of equilibrium plate thickness and temperature
- Thickness of seismogenic layer determined by depth to 700°C isothermal surface

Supporting Information:

Supporting Information may be found in the online version of this article.

Correspondence to:

M. C. Holdt and N. J. White,
mch74@cam.ac.uk;
njw10@cam.ac.uk

Citation:

Holdt, M. C., White, N. J., & Richards, F. D. (2025). Revised oceanic plate cooling models. *Journal of Geophysical Research: Solid Earth*, 130, e2024JB029890. <https://doi.org/10.1029/2024JB029890>

Received 10 JUL 2024

Accepted 14 JUN 2025

Author Contributions:

Conceptualization: M. C. Holdt, N. J. White, F. D. Richards
Data curation: M. C. Holdt, N. J. White, F. D. Richards
Formal analysis: M. C. Holdt, N. J. White, F. D. Richards
Funding acquisition: M. C. Holdt, N. J. White
Investigation: M. C. Holdt, N. J. White, F. D. Richards
Methodology: M. C. Holdt, N. J. White, F. D. Richards
Project administration: M. C. Holdt, N. J. White
Resources: M. C. Holdt, N. J. White, F. D. Richards
Software: M. C. Holdt, N. J. White, F. D. Richards
Supervision: N. J. White, F. D. Richards

© 2025. The Author(s).

This is an open access article under the terms of the [Creative Commons Attribution License](#), which permits use, distribution and reproduction in any medium, provided the original work is properly cited.

Revised Oceanic Plate Cooling Models

M. C. Holdt¹ , N. J. White¹ , and F. D. Richards² 

¹Bullard Laboratories, Department of Earth Sciences, University of Cambridge, Cambridge, UK, ²Department of Earth Science and Engineering, Imperial College London, London, UK

Abstract Global age-depth and heat flow observations provide constraints for cooling and subsidence of oceanic plates. Numerous studies have addressed this problem, which has a bearing upon the calibration of shear-wave tomographic models and upon lithospheric rheology. The robustness of these results depends upon the quality and spatial distribution of both age-depth and heat flow measurements. Here, we revisit the plate cooling model for two reasons. First, a database of 10,863 age-depth measurements that are distributed throughout the oceanic realm has been constructed. This database is combined with 3,573 heat flow measurements. Second, we wish to explore a range of analytical and numerical plate models that incorporate the temperature- and pressure-dependence of conductivity, of expansivity, and of specific heat capacity. Our goal is to identify plate models that jointly fit observational constraints, whilst honoring laboratory-based estimates of key thermal parameters. Both simple analytical and comprehensive numerical parameterizations recover an equilibrium plate thickness of 105 ± 10 or 96 ± 10 km with a temperature of $1,326 \pm 50^\circ\text{C}$. This recovered temperature is consistent with independent petrologic constraints. Spatial analysis of age-depth measurements demonstrates that previously invoked transient plate shallowing is not globally observed. This observation implies that the possible onset of a convective instability, which has been proposed as a mechanism to stabilize equilibrium plate thickness, might act on shorter length scales than that implied by previously reported transient shallowing. Finally, our revised plate model is used to track lithospheric thermal structure as a function of time and to calculate residual depth anomalies.

Plain Language Summary Earth's outermost layer, known as the lithosphere, comprises several interlocking tectonic plates. Throughout the oceans, seafloor is continuously created at mid-oceanic ridges, which are associated with high temperatures. When the new seafloor moves away from the mid-oceanic ridge, it gradually cools and sinks over many millions of years. Although this interesting problem has been studied by many scientists, it is always insightful to revisit it using modern measurements. Here, we use a newly assembled set of global depth and temperature measurements to revise the plate cooling model. Our results show that excellent fits to measurements can be achieved with both simple and comprehensive parameterizations. The plate model can be used to improve our understanding of the thermal structure of the Earth. It is also an essential starting point for calculating vertical deflection of the Earth's surface caused by the stirring of hot material that lies beneath the plates.

1. Introduction

It is generally accepted that oceanic lithosphere cools and subsides as a function of plate age (McKenzie, 1967; Turcotte & Oxburgh, 1967). This phenomenon is manifest by a combination of both age-depth and heat flow observations from the oceanic realm. Since the late 1960s, two principal classes of models have been developed to account for the evolution of oceanic lithosphere. Early studies suggested that a half-space cooling model accounts for age-depth observations (Davis & Lister, 1974; Takeuchi & Sakata, 1970). In this model, subsidence and heat flow are functions of the square root of crustal age. The half-space cooling model is based upon observations from relatively young (i.e., <80 Ma) oceanic crust and implicitly assumes that cooling and subsidence continue indefinitely with time. The observational database expanded when studies of oceanic magnetic anomalies enabled ages of subsidence anomalies on older oceanic crust to be dated (Hilde et al., 1976; Larson & Hilde, 1975; Vogt et al., 1971). Subsequently, Parsons and Sclater (1977) analyzed measurements from oceanic crust as old as 163 Ma and observed that the depth of seafloor that is older than ~ 80 Ma is shallower than that predicted by the half-space cooling model. They proposed that the plate model of McKenzie (1967), where temperature along a basal boundary of the cooling lithosphere is fixed to simulate resupply of heat, yields a better fit to a combination of age-depth and heat flow measurements. Stein and Stein (1992) built upon this pioneering analysis by jointly inverting an extensive

Validation: M. C. Holdt, N. J. White, F. D. Richards
Visualization: M. C. Holdt, N. J. White, F. D. Richards
Writing – original draft: M. C. Holdt, N. J. White, F. D. Richards
Writing – review & editing: M. C. Holdt, N. J. White, F. D. Richards

database of age-depth and heat flow measurements from the North Pacific Ocean and from the northwest Atlantic Ocean. It is now generally accepted that the plate model, rather than the half-space cooling model, provides a better description of the subsidence and heat flow characteristics of oceanic lithosphere. A significant drawback of the half-space cooling model is its inability to adequately fit age-depth and heat flow observations using a basal temperature that is consistent with independent petrologic and geochemical constraints (Hoggard et al., 2017).

In recent years, there has been considerable interest in developing and applying more physically realistic plate models that include, for example, temperature- and pressure-dependence of thermal parameters. McKenzie et al. (2005) showed that the thermal structure of the lithosphere can be constrained by using experimentally determined values of thermal conductivity, k , of thermal expansivity, α , and of specific heat capacity, C_p . Subsequent models have incorporated more physically accurate parameterizations, which include lithostatic pressure gradients, revised estimates of the radiative component of thermal conductivity, mineral phase transitions, hydrothermal circulation as well as an insulating crustal layer (Afonso et al., 2007; Grose & Afonso, 2013; T. Korenaga & Korenaga, 2016; Richards et al., 2018). Notwithstanding these developments, the success of a lithospheric thermal model still depends upon the ability to match a combination of age-depth and heat flow measurements. When jointly inverting these measurements, the robustness of an optimal model is predicated upon their quality and spatial distribution. A global database of age-depth observations assembled by Holdt et al. (2022) presents an opportunity to reassess the range of analytical and numerical plate models that have been proposed. It is important to acknowledge that the plate model is not universally accepted and that alternative oceanic cooling models have been proposed (Davies, 1988; Doin & Fleitout, 1996; Huang & Zhong, 2005; J. Korenaga, 2015; T. Korenaga et al., 2021).

Plate models typically recover values of temperature, T , lithospheric thickness, z_p , and in some cases ridge depth, z_r . For analytical models, T is defined as the temperature along the basal boundary of the lithosphere, T_b . In contrast, numerical models have a more flexible parameterization, which can be used to design more physically realistic temperature structures at and away from boundaries. In these schemes, which account for the isentropic temperature gradient of the convecting mantle, it is important to note that T refers to average potential temperature, T_p , not actual basal temperature (McKenzie & Bickle, 1988). z_p is the base of the oceanic lithosphere which is defined to consist of the mechanical boundary layer and part of the thermal boundary in accordance with McKenzie and Bickle (1988). It can also be regarded as an isothermal surface (see Priestley & McKenzie, 2013). Finally, z_r is defined as the global average depth of the mid-oceanic ridge axes that is isostatically corrected for sedimentary load and variable crustal thickness. Since there are independent constraints for these three parameters, the values recovered for the optimal plate model are testable.

The aims of this contribution are threefold. First, we test a variety of plate models by jointly inverting global databases of age-depth and heat flow measurements constructed by Holdt et al. (2022) and by Hasterok et al. (2011), respectively (Figure 1). These plate models include two simple analytical plate models and a more physically realistic temperature- and pressure-dependent parameterization. Our goal is to identify simple plate models that yield the best fit to observational constraints whilst also honoring independent petrologic and mineral physical constraints. Note that we specifically confine our attention to plate models and do not discuss alternative possibilities (e.g., T. Korenaga et al. (2021)). Second, we show that the transient shallowing for plate ages of 80–130 Ma that was observed by Crosby et al. (2006) and by several older studies is principally caused by an extensive plate-scale age-depth anomaly. Many positive and negative age-depth anomalies occur globally, which Holdt et al. (2022) and many previous authors have interpreted as the signal of mantle dynamic topography that is generated and maintained by convective processes. This observation highlights the importance of exploiting global age-depth and heat flow databases, which have improved spatial coverage. Finally, we use our results to infer possible scaling characteristics of the convective instability, whose existence has been invoked to stabilize plate thickness (Parsons & McKenzie, 1978). We conclude by revising the rheological properties of oceanic lithosphere that can be determined from the thermal structure calculated from plate models.

2. Observational Constraints

2.1. Age-Depth Measurements

Age-depth observations are a primary constraint for the plate and other models since they determine how oceanic lithosphere subsides as a function of time as a result of cooling and thickening. Here, we exploit a global database

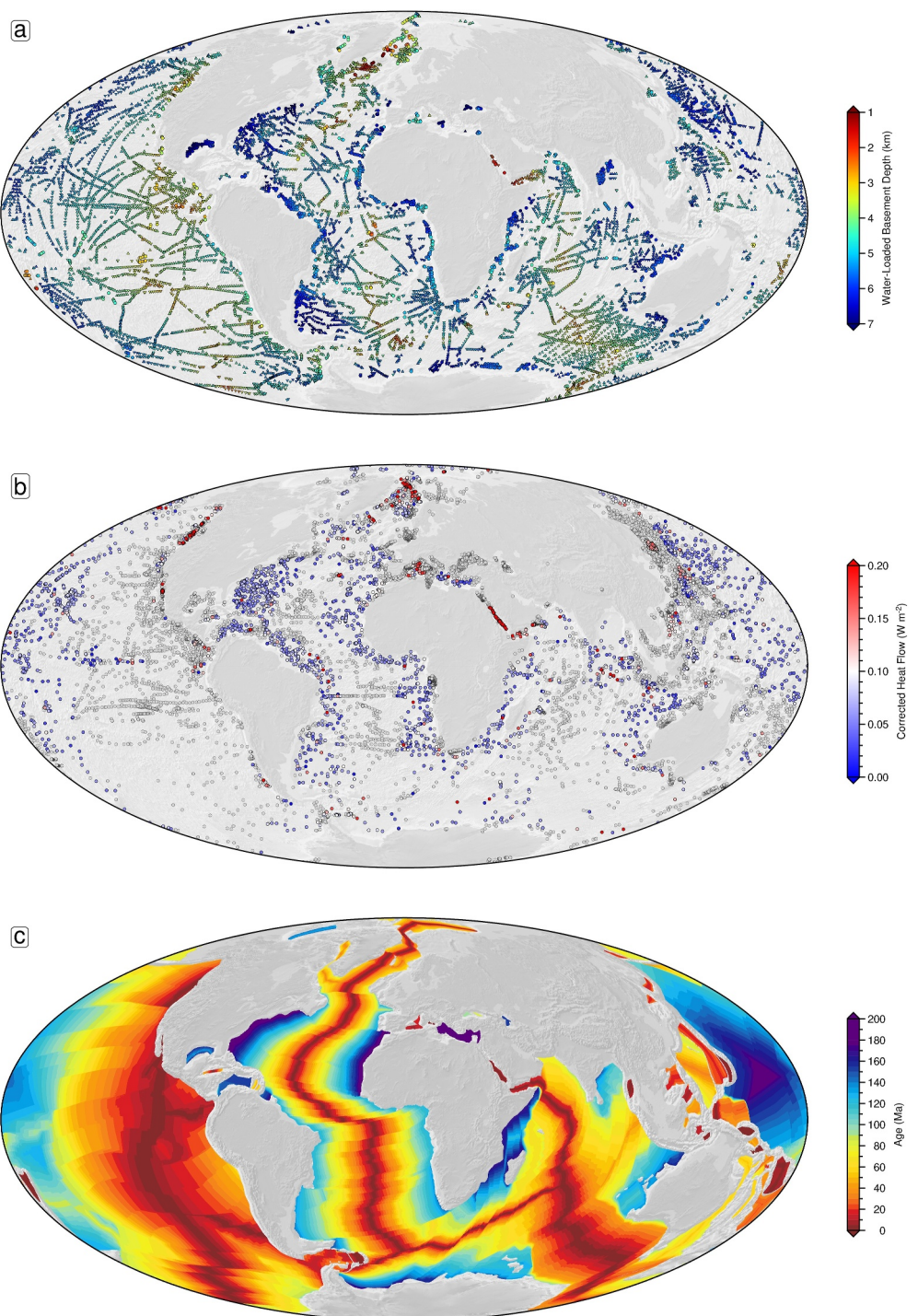


Figure 1. Global databases. (a) Distribution of water-loaded depth to oceanic basement measurements, averaged within 1° bins (Holdt et al., 2022). Circles = accurate measurements obtained by applying both sedimentary and crustal corrections; upward/downward pointing triangles = lower/upper estimates obtained by applying sedimentary correction and regional crustal correction. (b) Distribution of heat flow measurements (Hasterok et al., 2011). Colored/gray circles = measurements that pass/fail filtering process. (c) Augmented age grid of Seton et al. (2020) that includes modifications based upon regional studies compiled by Hoggard et al. (2017) and Holdt et al. (2022).

of water-loaded measurements of the depth to oceanic basement that was compiled by Holdt et al. (2022). This database contains 10,863 measurements and represents the largest compilation of accurately determined water-loaded estimates obtained from a combination of modern/legacy seismic reflection profiles and wide-angle experiments (Figure 1a). A combination of academic and commercial surveys was exploited. We note that Holdt et al. (2022) used the same global database to identify and measure the amplitudes and wavelengths of regional age-depth anomalies on many different spatial scales throughout the oceanic realm. They argue, along with many previous authors, that these anomalies can be regarded as a proxy for mantle dynamic topography. Here, our aims are different but related—we wish to use these age-depth observations together with global heatflow measurements to re-examine cooling and thickening of oceanic lithosphere. Although this problem has been exhaustively studied, we believe that our new global database can shed new and helpful insights.

Water-loaded depth to oceanic basement, w , is calculated as accurately as possible by carrying out two well-known corrections. The sedimentary correction, C_s , converts the variable thickness and density of the sedimentary load into an equivalent water load using the scheme described in detail by Hoggard et al. (2017) and subsequently revised by Holdt et al. (2022). The crustal correction, C_c , converts variable thickness and density of oceanic crust into a standard crustal reference column. The corrected depth to oceanic basement is given by $w = z_{sb} + C_s + C_c$ where z_{sb} is bathymetry. It is important to emphasize that C_s is generally more significant than C_c . From a global perspective, C_s is accurately determinable since ~70% of locations have sedimentary columns that are ≤ 0.5 km. Where crustal thickness and density are unknown, the value of C_c is gauged from regional crustal information, which yields either an upper or a lower bound for w . Table 1 lists the symbols and values of all parameters used within this study.

The database constructed by Holdt et al. (2022) represents a significant improvement in terms of both the quantity and the spatial distribution of accurate age-depth measurements. Previously constructed databases are often of only regional extent (see, e.g., Parsons & Sclater, 1977; Stein & Stein, 1992), rely upon gridded values whose accuracy is difficult to gauge (see, e.g., Crosby et al., 2006; Crosby & McKenzie, 2009), or are spatially biased toward continental margins (see, e.g., Richards et al., 2018). The revised and augmented database builds upon the detailed approach taken by Hoggard et al. (2017), primarily by interpreting substantial quantities of modern multi-channel and legacy single-channel seismic reflection profiles that criss-cross oceanic lithosphere of different ages. The inclusion of additional profiles dramatically improves spatial coverage throughout the oceanic realm. Age-depth measurements are always carried out on bona fide oceanic crust located away from anomalous tectonic features (e.g., seamounts, fracture zones, flexural moats). To aid spatial clarity, detailed measurements along individual profiles are binned every 1°. They are also assigned ages using a modern magnetic age grid (Seton et al., 2020; Figure 1c).

Figure 2a presents 10,863 age-depth measurements as a function of oceanic plate age. Note that more uncertain age-depth measurements from oceanic crust that is older than 200 Ma are omitted. This cloud of measurements has two significant characteristics. First, a mean relationship is evident, whereby subsidence decreases exponentially from ~2.5 to ~6 km as a function of plate age. Second, there is considerable but relatively uniform scatter about this mean relationship. The envelope of scatter is consistently ± 1 km, regardless of plate age. Since the pioneering work of Menard (1973), it is generally accepted that age-depth measurements that lie above or below the mean relationship represent positive and negative residual depth anomalies, respectively. These anomalies are interpreted as maximum signals of dynamic topography generated by mantle convective processes. For comparative purposes, Figure 2b shows these age-depth measurements binned every 2.5 Ma.

Previous plate model studies have sometimes attempted to minimize the influence of dynamic topography by excising regions dominated by dynamic topographic anomalies. For example, Crosby et al. (2006) exploited age-depth observations from regions, which featured near-zero (or at least minimal) gravity anomalies in order to avoid significant dynamic upwelling and downwelling. Goutorbe and Hillier (2013) removed age-depth measurements within the vicinity of major mantle plumes. Subsequently, Hoggard et al. (2016) used a global database of age-depth measurements which demonstrated that residual depth anomalies are ubiquitous down to wavelengths as short as 1,000 km. Here, we have not applied any such spatial filters. Instead, we assume that our database of 10,863 measurements represents a uniformly dense sampling of the oceanic realm so that dynamic upwellings and downwellings are potentially equally included over a complete range of plate ages (Holdt et al., 2022).

Table 1
Symbols and Values of Parameters

	Symbol	Parameter	Value	Units
Thermal parameters	α	Thermal expansivity	–	K ⁻¹
	C_p	Heat capacity	–	J K ⁻¹
	k	Thermal conductivity	–	W m ⁻¹ K ⁻¹
Recovered parameters	T	Mantle temperature	–	°C
	T_b	Mantle basal temperature	–	°C
	T_p	Mantle potential temperature	–	°C
	z_p	Equilibrium lithospheric thickness	–	km
	z_r	Water-loaded ridge depth	–	km
Observed subsidence	w	Water-loaded basement depth	–	km
	C_c	Crustal correction	–	km
	C_s	Sediment correction	–	km
	z_{sb}	Depth of seabed	–	km
Observed heat flow	H	Heat flow	–	W m ⁻²
	$\Delta T / \Delta z$	Thermal gradient	–	°C/m
	F	Perturbation of geotherm	–	dimensionless
	κ_s	Thermal diffusivity of sediment	0.25	mm ² s ⁻¹
	t_s	Duration of sedimentation	–	Ma
General	U	Sedimentation rate	–	km Ma ⁻¹
	t	Time	–	Ma
	z	Depth	–	km
	T	Temperature	–	°C
	P	Pressure	–	MPa
	X	Composition	–	
	ρ	Density	–	Mg m ⁻³
Calculated subsidence; calculated heat flow	ρ_m	Density of mantle at 0°C	3.30	Mg m ⁻³
	ρ_w	Density of water	1.03	Mg m ⁻³
	T_0	Surface temperature	0	°C
	κ	Thermal diffusivity	–	mm ² s ⁻¹
	ρ_b	Density at depth of compensation	–	Mg m ⁻³
	Δt	Time interval between nodes	–	Ma
	Δz_0^n	Depth interval between nodes	–	km
	k_0^n	Surface conductivity	–	W m ⁻¹ K ⁻¹
	T_0^n	Surface temperature	–	°C
Misfit calculation	T_1^n	Temperature at next deepest node	–	°C
	χ_s	Subsidence misfit	–	dimensionless
	χ_h	Heat flow misfit	–	dimensionless
	χ_t	Joint misfit	–	dimensionless
	w_i^o	Observed subsidence	–	km
	w_i^c	Calculated subsidence	–	km
	N_s	Number of subsidence age bins	65	dimensionless
	σ_i	Interquartile range of subsidence age bin	–	km
	H_i^o	Observed heat flow	–	W m ⁻²

Table 1
Continued

Symbol	Parameter	Value	Units
H_i^c	Calculated heat flow	—	W m^{-2}
N_h	Number of heat flow age bins	65	dimensionless
σ_i^*	Interquartile range of heat flow age bin		W m^{-2}

2.2. Heat Flow Measurements

Heat flow observations, which enable conductive heat loss through the surface of the lithospheric plate to be determined as a function of time, also help to constrain plate cooling. In the oceanic realm, standard heat flow measurements are acquired using a probe that is inserted into the sedimentary pile which measures temperature gradient and the in situ thermal conductivity (Sclater et al., 2014). Heat flow, H , is given by $H = k(\Delta T / \Delta z)$, where k is thermal conductivity, and $\Delta T / \Delta z$ is the thermal gradient between two points. A comprehensive global compilation of 23,428 heat flow observations was carefully compiled by Hasterok et al. (2011). This substantial undertaking provides an excellent complementary constraint for plate model considerations (Figure 1b).

Following the detailed methodology outlined by Hasterok et al. (2011) and by Richards et al. (2018), heat flow measurements are filtered and corrected. First, observations are edited by removing points which do not lie upon bona fide oceanic crust identified by a combination of linear magnetic anomalies and tripartite seismic structure, by deleting negative values and by binning the data at intervals of 0.1° to reduce the spatial bias associated with densely sampled locations. Second, measurements are excised if they lie between 0 and 65 Ma and have sedimentary thicknesses of less than 0.4 km. This filtering step is the most significant one since it excludes the majority of measurements from young oceanic crust. Although this filtering strategy reduces the number of measurements between 0 and 65 Ma, it is essential to isolate and remove any measurements that could be significantly perturbed by hydrothermal circulation, which primarily affects young oceanic crust (Hasterok, 2013;

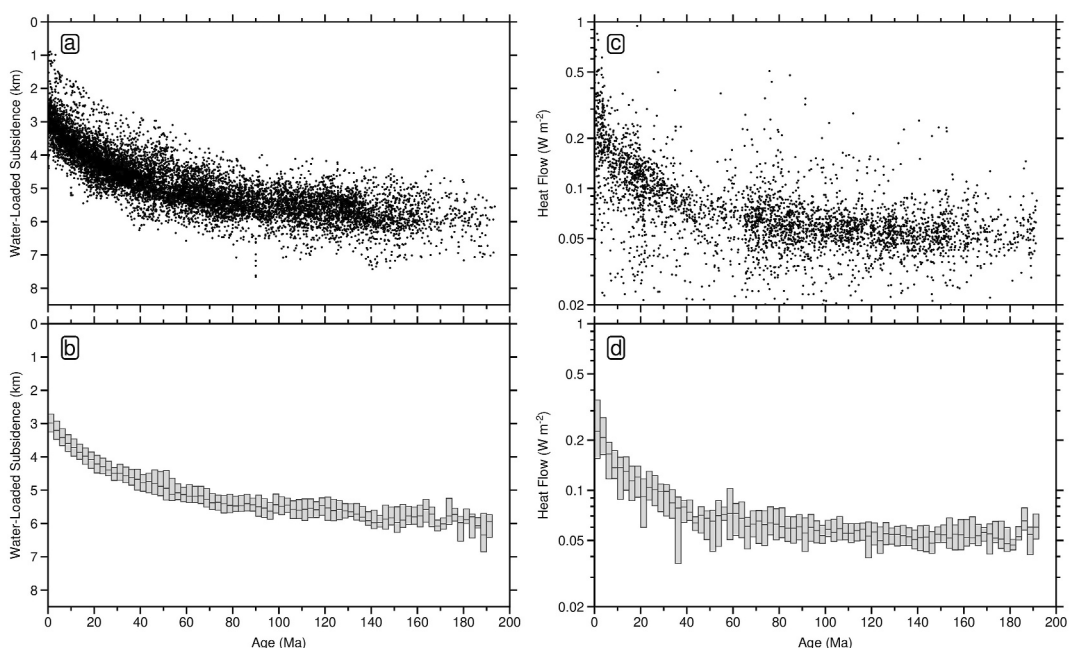


Figure 2. Age-depth and heat flow measurements as function of oceanic plate age. (a) Water-loaded measurements of depth to oceanic basement plotted as function of plate age and averaged within 1° bins (Holdt et al., 2022). See Figure 1a for global distribution. (b) Same measurements binned every 2.5 Ma. Horizontal bars with vertical gray boxes = median values with interquartile ranges. (c) Filtered and corrected heat flow measurements as function of plate age (Hasterok et al., 2011). See Figure 1b for global distribution. (d) Same measurements binned every 2.5 Ma. Horizontal bars with vertical gray boxes = median values with interquartile ranges.

Stein & Stein, 1992). For this specific purpose, sedimentary thicknesses are taken from the GlobSed global grid (Straume et al., 2019). Third, measurements are excised if they are within 60 km of seamounts or igneous plateaux. Locations of seamounts and large igneous provinces are taken from Wessel et al. (2010) and from Coffin and Eldholm (1994), respectively. Heat flow measurements from oceanic crust that is older than 200 Ma are omitted on two grounds. First, there are only ~ 10 measurements on oceanic crust beyond 200 Ma. Second, their values lie below the average value of 0.05 W m^{-2} at old plate ages. Finally, a sedimentation correction is applied in order to account for depression of the geothermal profile caused by rapid deposition. Reduced heat flow occurs since the initial temperature of uncompacted sediment is equal to that of bottom water. Assuming that the rate of sedimentation and the value of thermal diffusivity are constant as a function of time, Von Herzen and Uyeda (1963) calculated the fractional perturbation of the geothermal profile at the seabed, F , in the absence of internal heat generation. A simplified version of the analytical solution is given by

$$F = 1 + 2Y^2 \operatorname{erfc}(Y) - \operatorname{erf}(Y) - \frac{2Y}{\sqrt{\pi}} \exp(-Y^2), \quad (1)$$

where $Y = \frac{1}{2}Ut_s^{\frac{1}{2}}\kappa_s^{-\frac{1}{2}}$, U is the rate of sedimentation, t_s is the duration of sedimentation, and κ_s is thermal diffusivity of the sedimentary pile. Following Hasterok et al. (2011) and Richards et al. (2018), U is estimated by dividing sedimentary thickness by t_s , which is assumed to be equal to plate age. The impact of the sedimentation correction is relatively small. For example, 76% of measurements are corrected by $\leq 10\%$, when κ_s is assumed to be $0.25 \text{ mm}^2 \text{ s}^{-1}$. Following Richards et al. (2018), measurements from certain anomalous regions (e.g., Caspian Sea, Gulf of Mexico, Black Sea) are omitted because U significantly increased in these regions during Miocene times, violating the assumption of constant sedimentation rate (Galloway et al., 2011; Knapp et al., 2007; Sydorenko et al., 2017).

The application of this filtering and editing process yields a set of 3,573 heat flow measurements. Figure 2c presents corrected heat flow measurements as a function of oceanic plate age. Although there is considerable and variable scatter, a clear average relationship is visible. The average heat flow at mid-oceanic ridges is $\sim 0.25 \text{ W m}^{-2}$ and decreases exponentially to a value of $\sim 0.05 \text{ W m}^{-2}$ for the oldest oceanic lithosphere. For comparative purposes, these measurements have also been binned every 2.5 Ma (Figure 2d).

3. Modeling Strategy

The first detailed application of a plate model to age-depth and heat flow observations was carried out by Parsons and Sclater (1977) who derived appropriate partial differential equations, developed analytical solutions, and matched theory with observation. Their primary focus concerned fitting of age-depth observations from the North Pacific and North Atlantic oceans. They separately showed that their optimal plate model also matched limited heat flow observations. Subsequently, Stein and Stein (1992) employed a very similar analytical approach to jointly invert age-depth and heat flow observations. In both publications, the primary focus is recovery of basal temperature and equilibrium plate thickness. The critical underpinning thermal parameters are thermal conductivity, k , thermal expansivity, α , and isobaric specific heat capacity, C_p . Analytical solutions can be derived if these three parameters are assumed to be constant.

McKenzie et al. (2005) developed a more physically realistic version of the original plate model, which accounts for the temperature dependence of k , α and C_p , as well as isentropic decompression and melting of the mantle beneath the mid-ocean ridge in its initial temperature condition. This elaboration was motivated by the results of laboratory experiments, which clearly demonstrate that the values of these thermal parameters vary significantly over the temperature and pressure ranges observed within an olivine-dominated lithospheric mantle (Berman & Aranovich, 1997; Bouhifd et al., 1996; Hofmeister, 2010). Subsequent plate models have become increasingly sophisticated and, in general, are numerically solved in the absence of easily derived analytical solutions (Grose & Afonso, 2013; T. Korenaga & Korenaga, 2016; Richards et al., 2018).

Thermal evolution of oceanic lithosphere is calculated by solving the one-dimensional heat equation in a horizontally translating reference frame, reflecting the movement of the lithosphere away from the ridge axis. The general form of this equation is given by

$$\rho(T, P, X) C_p(T, X) \frac{\partial T}{\partial t} = \frac{\partial}{\partial z} \left[k(T, P, X) \frac{\partial T}{\partial z} \right], \quad (2)$$

where z is depth, t is time, and ρ is density, T is temperature, P is pressure and X is composition. In Equation 2, k and ρ depend upon T , P , and X . C_p primarily depends upon T and X since its pressure dependence is negligible over the range of pressures encountered within the lithosphere (Hofmeister, 2007).

If k , α and C_p are assumed to be constant, analytical solutions for subsidence and heat flow can be derived using standard Fourier expansion (Carslaw & Jaeger, 1959). Subsidence as a function of time, $w(t)$, is given by

$$w(t) = z_r + \frac{\rho_m \alpha (T - T_0) z_p}{2(\rho_m - \rho_w)} \left[1 - \frac{8}{\pi^2} \sum_{i=0}^N \frac{1}{(1+2i)^2} \exp - \frac{\kappa(1+2i)^2 \pi^2 t}{z_p^2} \right], \quad (3)$$

where $\kappa = k/\rho_m C_p$, ρ_m is density of mantle at 0°C, ρ_w is density of the water column, T is temperature of the basal boundary, $T_0 = 0^\circ\text{C}$ is surface temperature, and i is an integer whose maximum value is chosen to achieve convergence. Heat flow as a function of time, $H(t)$, is given by

$$H(t) = \frac{k(T - T_0)}{z_p} \left[1 + 2 \sum_{i=1}^N \exp \frac{-\kappa i^2 \pi^2 t}{z_p^2} \right]. \quad (4)$$

When comparing Equations 3 and 4, it is evident that, for a fixed w , a higher T requires a thinner z_p , and for a fixed H , a higher T requires a thicker z_p . If k , α and C_p vary as a function of pressure and temperature, $w(t)$ is calculated by numerically solving

$$w(t) = z_r + \frac{\rho_b}{\rho_m - \rho_w(t)} \int_0^{z_p} \left[1 - \frac{\rho(0, z')}{\rho(t, z')} \right] dz', \quad (5)$$

where z' is the Lagrangian depth co-ordinate that contracts as a result of lithospheric cooling, ρ_b is density at the depth of compensation which is defined as the depth down to which conductive cooling occurs (i.e., the shallowest depth where $\rho(t, z') = \rho(0, z')$), and $\rho_w(t) = 1.028 + 0.00424 w(t) \text{ Mg m}^{-3}$ to account for compressibility of the water column (Grose & Afonso, 2013). ρ_w increases as a function of time since the seabed deepens due to lithospheric cooling, which slightly amplifies the thickness of the water column, $w(t)$.

Heat flow, $H(t)$, is calculated using a finite-difference scheme which solves

$$H(n\Delta t) = \frac{k_0^n (T_1^n - T_0^n)}{\Delta z_0^n}, \quad (6)$$

where n is an integer, Δt is the time interval between nodes, Δz_0^n is the depth interval between nodes, k_0^n is surface conductivity, T_0^n is surface temperature, and T_1^n is temperature at the next node beneath the surface. In other words, $H(t)$ is calculated at the upper surface of the plate. Temperature-dependent models adopt parameterizations derived from experimental data on olivine. The temperature and pressure dependence of k , α and C_p have been determined using a range of different laboratory experiments on olivine, which are summarized in detail by Richards et al. (2020) where the necessary equations are given in their Appendix C ($k(P, T)$: Equation C.6; $\alpha(P, T)$: Equation C.9; and C_p : Equation C.4). Note that there are small but significant differences between the details of our thermal parameterization and those of Richards et al. (2018). For k , we use the parameterization of Pertermann and Hofmeister (2006) for dunite; for α , we use the parameterization of Bouhifd et al. (1996) presented in their Figure 3 (i.e., $\alpha_0 = 2.368 \times 10^{-5}$ and $\alpha_1 = 1.108 \times 10^{-8}$, not the values from their Table 2), and for C_p , we use the parameterization of Berman and Aranovich (1997), assuming an olivine composition of 89% forsterite and 11% fayalite where $c_0 = 1,611$, $c_1 = 12,484$ and $c_2 = 1729 \times 10^6$.

The insulating properties of oceanic crust can also be included. We adopt a pressure and temperature-dependent parameterization for k , α , and C_p for the insulating crustal layer (see Appendix C of Richards et al. (2018),

Equations C.11, C.12, and C.13). Following Grose and Afonso (2013) and Richards et al. (2018), a thin insulating crustal layer at the top of the cooling lithospheric plate is simulated by assuming, based upon petrologic analysis of oceanic drill core and mapping of ophiolites, that plagioclase is the dominant crystalline phase throughout the tripartite structure of oceanic crust (Carlson & Jay Miller, 2004; Dick et al., 2000; VanTongeren et al., 2021). Since plagioclase has a thermal conductivity which is $\sim 25\%$ that of olivine, oceanic crust can have a potentially significant insulating effect upon the underlying lithospheric mantle, provided that heat is transferred by conduction alone. A geometric mean is used to estimate the conductivity of an aggregate that comprises plagioclase, diopside and olivine (Grose & Afonso, 2013). This assumption yields an average crustal conductivity of $2.65 \text{ W m}^{-1} \text{ K}^{-1}$; Kelemen et al. (2004)).

4. Model Assessment and Benchmarking

Sets of subsidence and heat flow calculations are generated by systematically varying three key parameters: mantle temperature, T (equivalent to basal temperature, T_b , in our analytical models or potential temperature, T_p , in our numerical models); lithospheric thickness, z_p ; and ridge depth, z_r . Thus, T is varied between 1,100 and 1,600°C at increments of 25°C, z_p is varied between 60 and 160 km at increments of 5 km. z_r is generally assumed to be 2.5 ± 0.3 km but in some instances its value is varied between 2 and 3 km at increments of 0.05 km. In order to identify those models that yield optimal fits to age-depth and heat flow observations, the root mean squared (rms) misfit is calculated by carrying out parameter sweeps, which interrogate the three-dimensional misfit space. The formal misfit between observed and calculated subsidence, χ_s , is given by

$$\chi_s = \sqrt{\frac{1}{N_s} \sum_{i=1}^{N_s} \left(\frac{w_i^o - w_i^c}{\sigma_i} \right)^2}, \quad (7)$$

where w_i^o and w_i^c are observed and calculated values of water-loaded subsidence, N_s is the number of age bins, and σ_i is the interquartile range of each bin. The misfit between observed and calculated heat flow, χ_h , is given by

$$\chi_h = \sqrt{\frac{1}{N_h} \sum_{i=1}^{N_h} \left(\frac{H_i^o - H_i^c}{\sigma_i^*} \right)^2}, \quad (8)$$

where H_i^o and H_i^c are observed and calculated values of heat flow, N_h is the number of age bins, and σ_i^* is the interquartile range of each bin. Figure 2a shows that there is a noticeable reduction in the number of age-depth measurements older than 168 Ma, which contributes to a greater degree of uncertainty (Figure 2b). Following Richards et al. (2018), age-depth and heat flow measurements from oceanic crust that is older than 168 Ma are excluded to avoid spatial bias. Furthermore, measurements younger than 5 Ma can be omitted to mitigate the potential influence of hydrothermal circulation at the ridge axis (Grose & Afonso, 2013).

Following Stein and Stein (1992), we also interrogate the joint misfit between observed and calculated values of subsidence and heat flow, χ_t . For simplicity, equal weight is given to each set of observations so that

$$\chi_t = \sqrt{\left(\frac{\chi_s^2 + \chi_h^2}{2} \right)}. \quad (9)$$

We wish to revisit a range of both analytical and numerical plate models by using a combination of subsidence modeling, heat flow modeling and joint modeling. The purpose of investigating these different forms of modeling is to probe differences between proposed models in the context of the self-consistency of subsidence and heat flow measurements. In each case, we are interested in locating a global minimum which identifies the optimal values of T , z_p and sometimes z_r . We are also interested in exploring any obvious trade-offs between these three parameters. Recovered values of these plate parameters are benchmarked against independent geologic constraints. For example, ambient mantle potential temperature has been estimated from petrologic and geochemical studies at mid-oceanic ridges (e.g., 1,250–1,350°C: Katsura et al., 2004; 1,280–1,400°C: Herzberg et al., 2007;

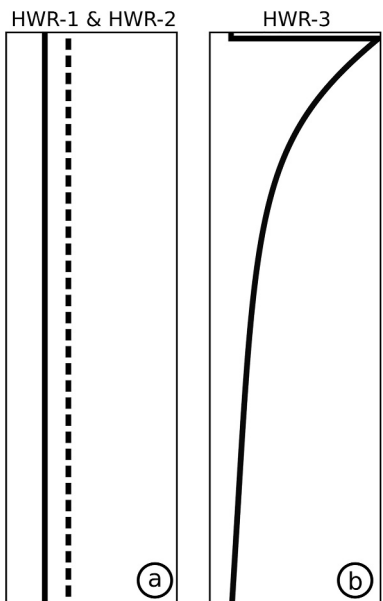


Figure 3. Cartoons showing different thermal conductivity parameterizations. (a) Models HWR-1 and HWR-2 where thermal conductivity is constant with depth; solid line = HWR-1; dashed line = HWR-2. Thermal conductivity is scaled between 2 and $7 \text{ W m}^{-1} \text{ K}^{-1}$. (b) Model HWR-3 where thermal conductivity varies as function of depth according to Pertermann and Hofmeister (2006) with insulating crustal layer (Grose & Afonso, 2013).

z_r as a quasi-independent parameter that can be extracted by interrogating the joint misfit between observed and calculated subsidence and heat flow. In these instances, recovered values of z_r do not differ significantly from 2.5 km.

5. Results

5.1. Original Analytical Model (HWR-1)

Figure 4 presents the results of an analytical plate model, which adopts the exact parameterization assumed by Parsons and Sclater (1977). Using this legacy parameterization has two purposes. First, we wish to examine the effects of increasing the number and distribution of subsidence measurements upon this parameterization. Second, we wish to investigate the impact of separately and jointly modeling subsidence and heat flow data (Figures 4a and 4b). In their scheme, the value of mean thermal conductivity, $k = 3.138 \text{ W m}^{-1} \text{ K}^{-1}$, is based upon the laboratory experiments of Schatz and Simmons (1972), schematically shown in Figure 3a. The value of mean heat capacity, $C_p = 1,171.52 \text{ J K}^{-1}$, is based upon measurements of typical minerals over a temperature range that is appropriate for oceanic lithosphere (Goranson, 1942). Note that Parsons and Sclater (1977) varied thermal expansivity to minimize the misfit between observed and calculated subsidence measurements. Their recovered value for combined subsidence modeling of the North Pacific and North Atlantic oceans is $\alpha = (3.2 \pm 1.1) \times 10^{-5} \text{ K}^{-1}$.

Our modeling strategy is implemented in three steps. First, subsidence observations alone were fitted by systematically varying T and z_p where z_r is fixed at 2.5 km. There is a weak global minimum at $\chi_s < 0.2$ with a clear negative trade-off between T and z_p such that a thinner, hotter plate or a cooler, thicker plate fits the observations equally well (Figure 4c). At the global minimum, $T = 1,375^\circ\text{C}$ and $z_p = 106 \text{ km}$. In comparison, Parsons and Sclater (1977) obtained $T = 1,350^\circ\text{C}$ and $z_p = 125 \text{ km}$. Minor differences reflect the fact that Parsons and Sclater (1977) exploit 377 age-depth measurements from the North Pacific and North Atlantic oceans whereas our global database contains 10,863 measurements. Comparison of Figures 4a and 4f shows that the average slope of their 377 measurements is slightly steeper. Although this difference is small, it acts to displace our estimates of T

$1,350 \pm 50^\circ\text{C}$: Lee et al., 2009; $1,318^{+44}_{-32}^\circ\text{C}$: Matthews et al., 2016). Dalton et al. (2014) provide a petrologic range of $1,300$ – $1,550^\circ\text{C}$, which they refine to a range of $1,314$ – $1,464^\circ\text{C}$ (i.e., $1,388 \pm 45^\circ\text{C}$) by including constraints provided by seismic velocity values and zero-age depths. The midpoint and range that qualitatively honors the common overlaps between these different estimates is $1,332 \pm 18^\circ\text{C}$.

From a geodynamic perspective, equilibrium lithospheric thickness is a useful and important concept. However, it is difficult to independently and accurately constrain its value because the relationship between long-term mechanical properties and, say, seismic velocity is unclear. Some studies have either implicitly or explicitly estimated z_p by calibrating shear wave tomographic models against a plate cooling model, which, from the perspective of this contribution, represents a circular argument (Priestley & McKenzie, 2006; Priestley et al., 2024). Steinberger and Becker (2018) determine lithospheric thickness from the results of five earthquake tomographic models by identifying the depth to an empirically estimated isothermal surface (i.e., $1,126^\circ\text{C}$). They obtain a mean thickness of equilibrium oceanic lithosphere of $109 \pm 22 \text{ km}$. Burgos et al. (2014) use the results of a global surface wave dispersion study to suggest that the lithosphere–asthenosphere boundary beneath old oceanic plates commences at a depth of $\sim 100 \text{ km}$.

Although the zero-age depth at mid-oceanic ridges can be determined directly from subsidence observations, its average value is difficult to pinpoint since depths of mid-oceanic ridges vary by $\pm 1 \text{ km}$ or more, principally as a consequence of mantle dynamic topography. It is generally agreed that the mean global value is $z_r = 2.5 \pm 0.3 \text{ km}$ which is what we use here (Parsons & Sclater, 1977; Rowley, 2019; Stein & Stein, 1992). Occasionally, we treat

that can be extracted by interrogating the joint misfit between observed and

calculated subsidence and heat flow. In these instances, recovered values of z_r do not differ significantly from

2.5 km.

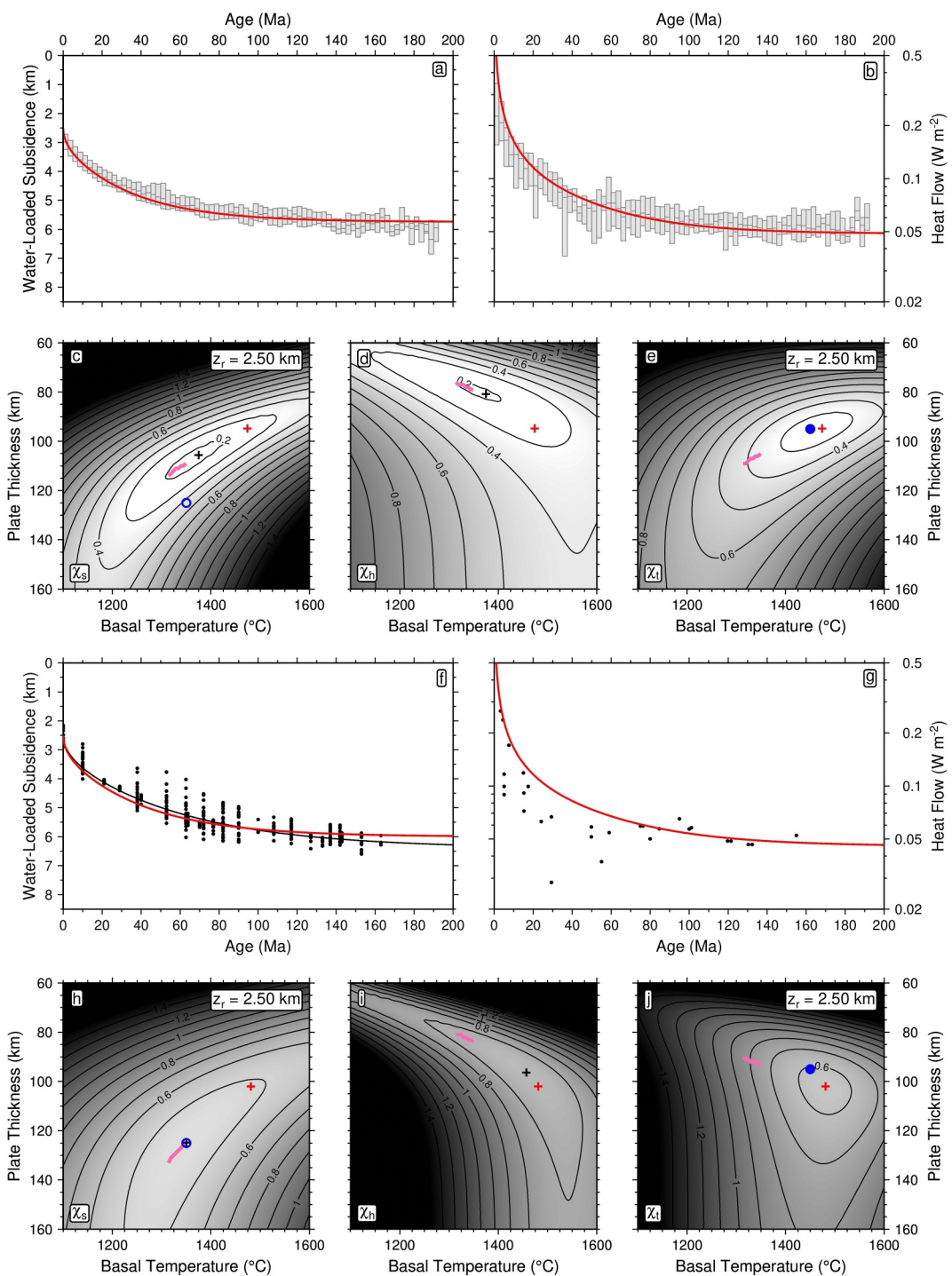


Figure 4.

and z_p to higher and thinner values, respectively. Second, heat flow observations are fitted. In this case, we obtain $T = 1375^\circ\text{C}$ and $z_p = 81$ km (i.e., a thinner plate; Figure 4d).

Finally, we jointly fit subsidence and heat flow observation which yields $T = 1,474^\circ\text{C}$ and $z_p = 95$ km at the global minimum of $\chi_t = 0.248$ (Figure 4e). This joint fitting yields a temperature that is $\sim 100^\circ\text{C}$ hotter and a thinner plate. Figure 4e demonstrates that Stein and Stein (1992) obtained very similar values of $T = 1,450^\circ\text{C}$ and $z_p = 95$ km with a thermal expansion coefficient of $\alpha = 3.1 \times 10^{-5} \text{ K}^{-1}$. Although they exploited different global databases of subsidence and heat flow measurements, the principal reason for this close similarity is the fact that, in both cases, joint fitting of subsidence and heat flow observations has been carried out assuming $k = 3.138 \text{ W m}^{-1} \text{ K}^{-1}$, which results in a thinner, hotter plate.

Figures 4f and 4g show the original subsidence and heat flow measurements of Parsons and Sclater (1977). These observations include 377 age-depth measurements and 29 heat flow measurements. Figure 4h demonstrates that the global minimum obtained by fitting subsidence measurements occurs at $T = 1,350^\circ\text{C}$ and $z_p = 125$ km (i.e., identical to the values recovered by Parsons and Sclater (1977)). However, Figure 4i demonstrates that the global minimum obtained by fitting heat flow observations occurs at $T = 1,457^\circ\text{C}$ and $z_p = 96$ km. Note that, in this case, misfit was only calculated using heat flow measurements >60 Ma in order to negate the influence of hydrothermal circulation which affects young oceanic crust. Similarly, joint modeling yields $T = 1,481^\circ\text{C}$ and $z_p = 102$ km (Figure 4j). This result highlights the fact that combined modeling of subsidence and heat flow measurements tends to generate an optimal model with an excessively high temperature (see also Stein & Stein, 1992). This result is a direct consequence of formally fitting heat flow measurements, which Parsons and Sclater (1977) did not implement although they did use their subsidence-based model to predict heat flow variation.

In summary, there are two obvious problems that are highlighted by our three-step analysis (Figure 4). First, parameter values recovered by separately fitting subsidence and heat flow observations are strikingly different—subsidence observations tend to predict a thicker plate and heat flow observations predict a thinner plate. Second, joint fitting of subsidence and heat flow measurements does not yield parameter values that are consistent with independent constraints, particularly with respect to the recovered basal temperature which is $\sim 150^\circ\text{C}$ hotter than expected. This exceptionally hot basal temperature is strongly influenced by the fitting of heat flow measurements, which yields a very thin plate (<100 km) for all basal temperatures.

5.2. Revised Analytical Model (HWR-2)

The mismatch between parameter values recovered from both separate and joint modeling of subsidence and heat flow measurements indicates that the original parameterization of Parsons and Sclater (1977) requires some modification. This mismatch arises because, for a given geothermal profile, subsidence is sensitive to the average value of thermal conductivity that is obtained by integration over the total thickness of the cooling lithosphere whereas surface heat flow is more sensitive to the value of thermal conductivity toward the top of the lithosphere (compare Equations 3 and 4).

The value of k assumed by Parsons and Sclater (1977) is $3.138 \text{ W m}^{-1} \text{ K}^{-1}$. It is a mean value for the upper 120 km of the mantle (Schatz & Simmons, 1972). The simplest approach is to identify a suitable average value of

Figure 4. Analytical plate model using Parsons and Sclater (1977) parameterization (HWR-1). (a) Horizontal bars with vertical gray boxes = median values with interquartile ranges of age-depth measurements; red line = optimal fit between observed and calculated age-depth obtained by jointly fitting age-depth and heat flow measurements where $T = 1,474^\circ\text{C}$ and $z_p = 95$ km, when z_r is fixed at 2.50 km. (b) Horizontal bars with vertical gray boxes = median values with interquartile ranges of heat flow measurements; red line = optimal fit between observed and calculated heat flow obtained by jointly fitting age-depth and heat flow measurements. (c) Misfit between observed and calculated age-depth, χ_s , plotted as function of basal temperature and plate thickness when z_r is fixed at 2.50 km. Black cross = locus of global minimum; red cross = locus of global minimum shown in panel (e); open blue circle = locus of global minimum obtained by Parsons and Sclater (1977); pink line = loci of minima when basal temperature is fixed at $1,332 \pm 18^\circ\text{C}$. (d) Misfit between observed and calculated heat flow, χ_h . (e) Joint misfit between observed and calculated age-depth and heat flow, χ_t , when z_r is fixed at 2.50 km. Red cross = global minimum at $T = 1,474^\circ\text{C}$; $z_p = 95$ km; Blue circle = locus of global minimum obtained by Stein and Stein (1992). (f) Black circles = original age-depth measurements of Parsons and Sclater (1977) from North Pacific and North Atlantic Oceans; red line = optimal fit between observed and calculated age-depth obtained by jointly fitting age-depth and heat flow measurements of Parsons and Sclater (1977) where $T = 1,481^\circ\text{C}$ and $z_p = 102$ km, when z_r is fixed at 2.50 km; black line = optimal fit between observed and calculated age-depth obtained by Parsons and Sclater (1977) where $T = 1,350^\circ\text{C}$; $z_p = 125$ km; $z_r = 2.50$ km. (g) Black circles = original heat flow measurements of Parsons and Sclater (1977); red line = optimal fit between observed and calculated heat flow obtained by jointly fitting age-depth and heat flow measurements of Parsons and Sclater (1977). (h)–(j) Same as panels (c)–(e) where misfit is calculated using age-depth and heat flow measurements shown in panels (f) and (g).

k , which can reconcile the mismatch that has arisen by systematically varying k between 3.20 and 4.10 $\text{W m}^{-1} \text{K}^{-1}$ at intervals of 0.1 $\text{W m}^{-1} \text{K}^{-1}$. For $k = 3.8 \text{ W m}^{-1} \text{K}^{-1}$, a global minimum of $\chi_i = 0.247$, obtained by jointly fitting subsidence and heat flow observations, is located at $T = 1,326^\circ\text{C}$ and $z_p = 105 \text{ km}$ when z_r is fixed at 2.5 km (Figures 3a and 5a–5e). This average value of k falls within the bounds of experimental and geologic uncertainty (see, e.g., Grose & Afonso, 2013; Richards et al., 2018; Figure 6a).

In contrast to the HWR-1 plate model, the recovered value of $T = 1,326^\circ\text{C}$ is now in excellent agreement with that determined from independent petrologic and geochemical studies (i.e., $T_p = 1,332 \pm 18^\circ\text{C}$; Figure 5e). A slightly higher value of mean thermal conductivity is justified by examining experimental measurements (Hofmeister, 1999, 2005; Pertermann & Hofmeister, 2006). For example, Pertermann and Hofmeister (2006) use a laser flash technique which yields higher thermal conductivity values throughout the lithosphere compared with the original measurements of Schatz and Simmons (1972). The mean thermal conductivity for temperatures between 0 and 1300°C from laser flash experiments is $k = 3.6 \text{ W m}^{-1} \text{K}^{-1}$ (Figure 6a). This value assumes no radiative component which, if included, could significantly increase the mean thermal conductivity of the lithosphere. The recovered value of lithospheric thickness, $z_p = 105 \pm 10 \text{ km}$, equates to a thickness of $\sim 90 \text{ km}$ for a basal temperature of 1,126°C which is at the lower bound of, but still broadly consistent with, independent estimates of equilibrium lithospheric thickness ($z_p = 109 \pm 22 \text{ km}$; Steinberger & Becker, 2018). Priestley et al. (2024) constructed steady state geothermal profiles from temperature estimates, which were obtained by calibrating global shear-wave velocity measurements. At one location on old Pacific oceanic crust ($\sim 140 \text{ Ma}$), their calculated lithospheric thickness (equivalent to equilibrium plate thickness) is 104 km.

In order to sidestep any possible effects of efficient hydrothermal circulation close to the ridge axis, we match the approach of Richards et al. (2018) by excluding subsidence and heat flow observations from seafloor younger than 5 Ma. We also fix the value of z_r at 2.5 km. Critically, the effects of fixing z_r and of excluding measurements from the youngest lithosphere are easily tested. First, we allow z_r to vary, which yields $T = 1,349^\circ\text{C}$, $z_p = 105 \text{ km}$ and $z_r = 2.45 \text{ km}$ (Figures 5f–5h). Second, we can then include subsidence values younger than 5 Ma, which yields $T = 1,347^\circ\text{C}$, $z_p = 106 \text{ km}$ and $z_r = 2.45 \text{ km}$ (Figures 5i–5k). In both cases, the recovered values of T still agree with those estimated from independent petrologic and geochemical studies (i.e., $T_p = 1,332 \pm 18^\circ\text{C}$). The recovered values for z_p are almost identical. We conclude that permitting the value of z_r to vary yields a slightly higher T whilst excluding measurements from seafloor that is younger than 5 Ma has no discernible influence upon the recovered plate model.

5.3. Temperature- and Pressure-Dependent Model (HWR-3)

Notwithstanding the fact that the simple HWR-2 analytical model yields an excellent fit between observed and calculated values of subsidence and heat flow, we acknowledge that there is some interest in developing more sophisticated (i.e., physically realistic) plate models. One reason concerns the detailed temperature structure of the evolving plate, which can change significantly depending upon the specific thermal parameterization employed. For example, the recovered temperature structure can influence the empirical relationship between temperature and shear wave velocity (Priestley & McKenzie, 2006).

The starting point concerns the results of laboratory experiments, which clearly demonstrate that α , k , and C_p vary as a function of temperature and pressure (Figure 6; McKenzie et al., 2005; Richards et al., 2018). Here, we use a modified version of the temperature- and pressure-dependent parameterization implemented by Richards et al. (2018), which itself is a revised version of earlier parameterizations developed by McKenzie et al. (2005) and by Grose and Afonso (2013). A useful summary of laboratory experiments is provided by Figure 7 of Richards et al. (2020). Our changes are as follows—the temperature-dependence of k is based on the lattice conductivity with a negligible radiative component (Figures 3c and 6a); the temperature-dependence of α is taken from Figure 3 of Bouhifd et al. (1996) rather than from their Table 2 (values quoted in table and shown in figure are mutually inconsistent; Figure 6b); and the parameterization of C_p is chosen so that olivine consists of 89% forsterite and 11% fayalite (Berman & Aranovich, 1997; Figure 6c). Figure 6 is a schematic summary of the chosen parameterization, the details of which are described in considerable detail by Richards et al. (2020). Oceanic crust is assumed to act as an insulating layer in accordance with Grose and Afonso (2013). However, we reduce the average crust thickness to 6.4 km in accordance with Christeson et al. (2019) and with Holdt et al. (2022).

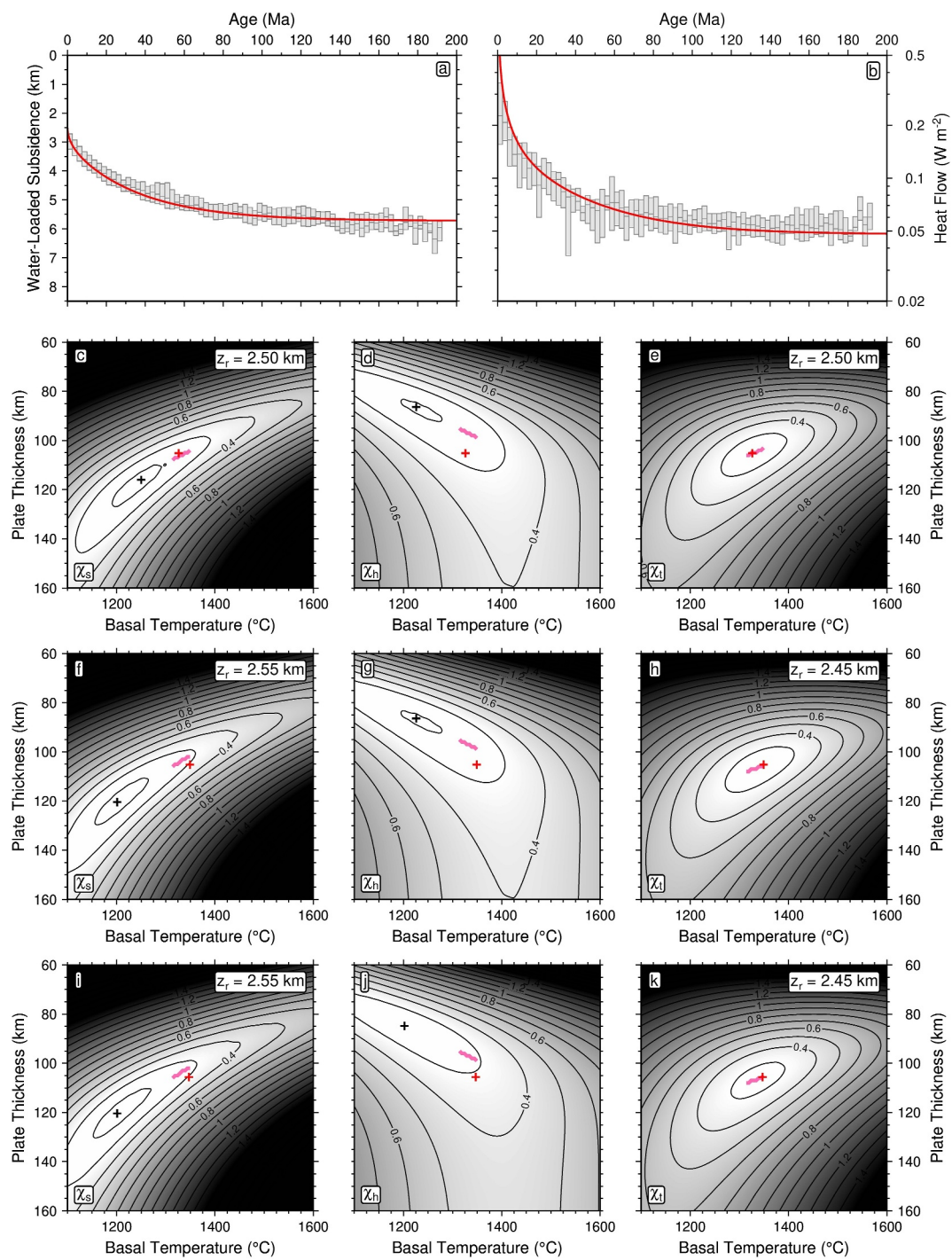


Figure 5.

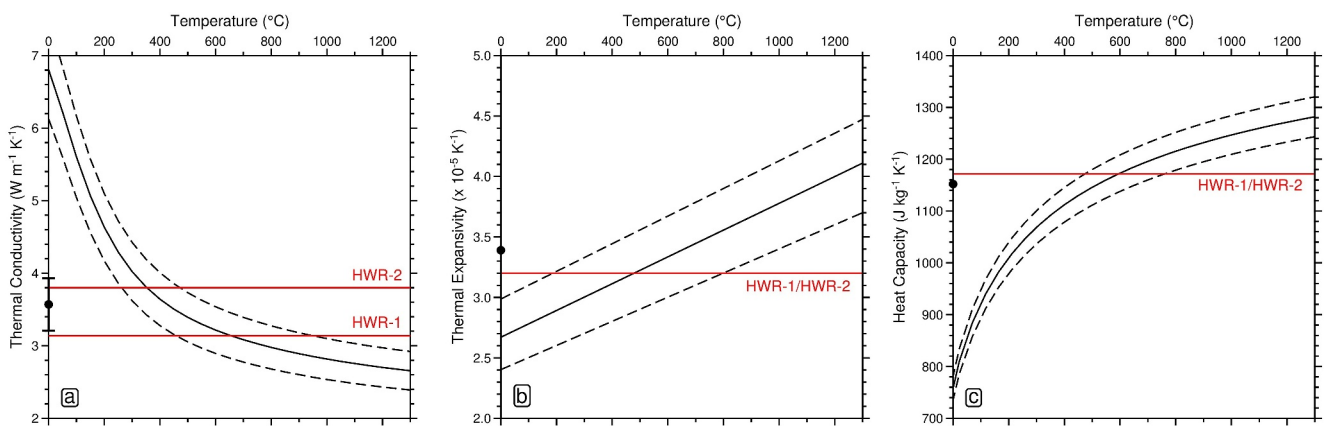


Figure 6. Plate model parameterization. (a) Thermal conductivity plotted as function of temperature. Solid/dashed black lines = forsterite lattice conductivity measurements $\pm 10\%$ uncertainty at constant pressure of 0.1 MPa, redrawn from Pertermann and Hofmeister (2006); red lines = constant thermal conductivities assumed for HWR-1 and HWR-2; black circle with uncertainty = mean thermal conductivity value calculated between 0 and 1,300°C, based upon parameterization of Pertermann and Hofmeister (2006) with $\pm 10\%$ uncertainty. (b) Thermal expansivity plotted as function of temperature. Solid/dashed black lines = thermal expansivity measurements $\pm 1\sigma$ for constant pressure of 0.1 MPa, taken from Figure 3 of Bouhifd et al. (1996); red line = constant thermal expansivity assumed for HWR-1 and HWR-2 models; black circle = mean thermal expansivity value calculated between 0 and 1,300°C, based upon parameterization of Bouhifd et al. (1996). (c) Heat capacity plotted as function of temperature. Solid/dashed black lines = heat capacity measurements $\pm 3\%$ uncertainty using parameterization of Berman and Aranovich (1997), which assumes 89% forsterite and 11% fayalite; red line = constant heat capacity assumed for HWR-1 and HWR-2 models; black circle = mean heat capacity value calculated between 0 and 1,300°C, based upon parameterization of Berman and Aranovich (1997).

A revised plate model is presented in Figure 7. An optimal model obtained by jointly fitting subsidence and heat flow observations is located at $T = 1,326^\circ\text{C}$, $z_p = 96$ km and $z_r = 2.80$ km where $\chi_t = 0.195$. In this instance, the value of z_r is also obtained by optimization. From the perspective of statistical tolerance, this result is in close agreement with that obtained using the HWR-2 analytical model. Note that the decrease in the value of χ_t is statistically insignificant, that the decrease in equilibrium plate thickness from 105 to 96 km is minor, and that there is no change in the value of T . The recovered value of z_r falls within the range of observed mean ridge depth values (i.e., 2.5 ± 0.3 km).

6. Discussion

Databases of age-depth and heat flow measurements can be satisfactorily fitted using any one of the three models presented here. Both the HWR-2 and HWR-3 models recover basal and potential temperatures that honor independent petrologic constraints. The significant reduction in the recovered basal temperature value between the HWR-1 model ($T = 1474^\circ\text{C}$) and the HWR-2 model ($T = 1326^\circ\text{C}$) highlights the sensitivity of any plate model to the parameterization of conductivity. Compared with HWR-3, HWR-2 is clearly a very simple model in terms of parameterization. Although k , α and C_p vary as a function of temperature and, to a lesser extent, pressure, both plate subsidence and heat flow principally depend upon integrated averages of these parameters. In other words, unlike seismic constraints on thermal structure, these surface observations are largely (but not entirely) insensitive to the detailed functional variation of each parameter. The HWR-3 model adopts a more sophisticated parameterization, which incorporates the temperature- and pressure-dependence of k , α and C_p . Laboratory results

Figure 5. Revised analytical plate model with increased thermal conductivity (HWR-2). (a) Horizontal bars with vertical gray boxes = median values with interquartile ranges of age-depth measurements; red line = optimal fit between observed and calculated age-depth obtained by jointly fitting age-depth and heat flow measurements where $T = 1,326^\circ\text{C}$ and $z_p = 105$ km, when z_r is fixed at 2.50 km. (b) Horizontal bars with vertical gray boxes = median values with interquartile ranges of heat flow measurements; red line = optimal fit between observed and calculated heat flow obtained by jointly fitting age-depth and heat flow measurements. (c) Misfit between observed and calculated age-depth, χ_s , plotted as function of basal temperature and plate thickness when z_r is fixed at 2.50 km. Black cross = locus of global minimum; red cross = locus of global minimum shown in panel (e); pink line = loci of minima when basal temperature is fixed at $1,332 \pm 18^\circ\text{C}$. Note that age-depth measurements between 0 and 5 Ma are excluded, and the ridge depth is fixed at 2.50 km. (d) Misfit between observed and calculated heat flow, χ_h . Note that heat flow measurements between 0 and 5 Ma are excluded. (e) Joint misfit between observed and calculated age-depth and heat flow, χ_t , when z_r is fixed at 2.50 km. (f)–(h) Same as panels (c)–(e) except that z_r is variable. Note that locus of global minimum obtained by jointly fitting age-depth and heat flow measurements shifts very slightly to $T = 1,349^\circ\text{C}$; $z_p = 105$ km; $z_r = 2.45$ km. (i)–(k) Same as panels (c)–(e) except that z_r is variable, and both age-depth and heat flow measurements between 0 and 5 Ma are now included. Note that locus of global minimum obtained by jointly fitting age-depth and heat flow measurements shifts very slightly to $T = 1,347^\circ\text{C}$; $z_p = 106$ km; $z_r = 2.45$ km.

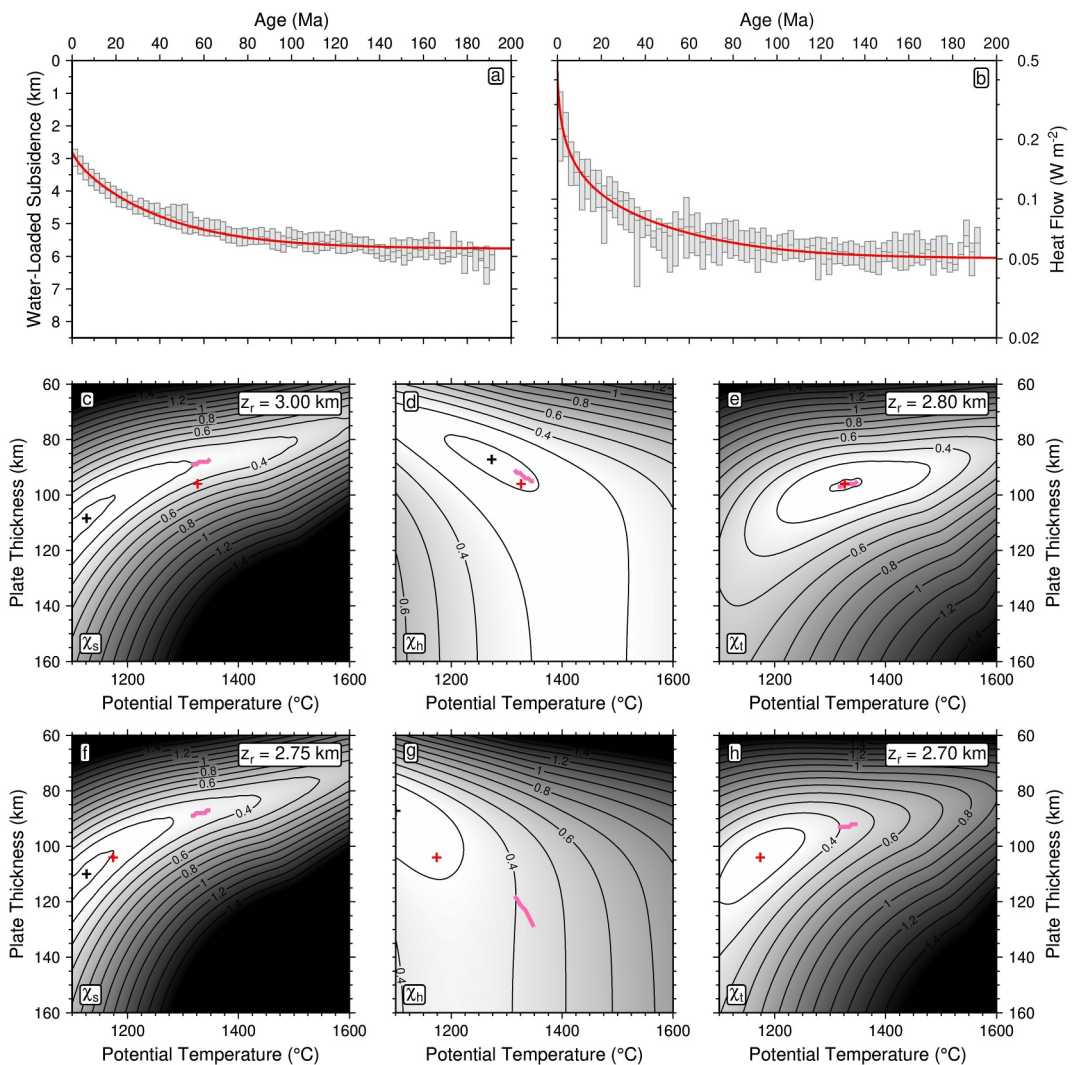


Figure 7. Plate model with temperature- and pressure-dependent parameters (HWR-3). (a) Horizontal bars with vertical gray boxes = median values with interquartile ranges of age-depth measurements; red line = optimal fit between observed and calculated age-depth obtained by jointly fitting age-depth and heat flow measurements where $T = 1,326^\circ\text{C}$; $z_p = 96 \text{ km}$; $z_r = 2.80 \text{ km}$. (b) Horizontal bars with vertical gray boxes = median values with interquartile ranges of heat flow measurements; red line = optimal fit between observed and calculated heat flow obtained by jointly fitting age-depth and heat flow measurements. (c) Misfit between observed and calculated age-depth, χ_s , plotted as function of basal temperature and plate thickness for $z_r = 3.00 \text{ km}$. Black cross = locus of global minimum; red cross = locus of global minimum shown in panel (e); pink line = loci of minima when basal temperature is fixed at $1,332 \pm 18^\circ\text{C}$. (d) Misfit between observed and calculated heat flow, χ_h . (e) Joint misfit between observed and calculated age-depth and heat flow, χ_j , for $z_r = 2.80 \text{ km}$. (f)–(h) Same as panels (c)–(e) except that insulating oceanic crustal layer is not included. In this case, optimal fit obtained by jointly fitting age-depth and heat flow measurements yields $T = 1,174^\circ\text{C}$; $z_p = 104 \text{ km}$; $z_r = 2.70 \text{ km}$. Note that basal temperature is expressed here as potential temperature since adiabatic gradient is included for HWR-3 (Richards et al., 2018).

obtained using either the contact method or laser flash analysis show that k increases significantly at low temperatures (i.e., $5.5\text{--}7.0 \text{ W m}^{-1} \text{ K}^{-1}$; (Perermann & Hofmeister, 2006; Schatz & Simmons, 1972)). This increase perturbs the recovered value of basal temperature, pushing it outside the independently accepted range (Figure 7h). One solution is incorporation of an insulating crust whose thermal properties remain, in turn, uncertain (see Figure 7a of Richards et al. (2018) for further details). The addition of an insulating crustal layer increases the recovered basal temperature from $T = 1,174^\circ\text{C}$ to $T = 1,326^\circ\text{C}$ (Figures 7e–7h). This change demonstrates the sensitivity of plate models to the adopted conductivity structure, especially when fitting heat

Table 2
Reference Models for Evolution of Oceanic Lithosphere

Name	Reference	Location	w	H	k	α	C_p	T	z_p	z_r
PSM	Parsons and Sclater (1977)	N.Pac., N.Atl.	377	29	3.138	3.20	1,171.52	1,350	125	2.50
GDH1	Stein and Stein (1992)	N.Pac., NW.Atl.	Grid	5,539	3.138	3.10	1,171.52	1,450	95	2.60
CHABLIS	Doin and Fleitout (1996)	Global	Grid	853	3.100	4.20	1,124.00	1,310	105	2.50
HW05	Hillier and Watts (2005)	N.Pacific	Grid	Grid	3.371	2.77	1,171.52	1,363	120	3.01
MJP05	McKenzie et al. (2005)	N/A	N/A	N/A	V	V	V	1,315	106	2.50
CMS06	Crosby et al. (2006)	N.Pacific	Grid	N/A	V	V	V	1,315	90	2.65
CM09	Crosby and McKenzie (2009)	Global	Grid	N/A	V	V	V	N/A	90	2.60
RHWC18	Richards et al. (2018)	Global	2,028	3,597	V	V	V	1,302	136	2.64
HWR-1	This study	Global	10,863	3,573	3.138	3.20	1,171.52	1,474	95	2.50
HWR-2	This study	Global	10,863	3,573	3.800	3.20	1,171.52	1,326	105	2.50
HWR-3	This study	Global	10,863	3,573	V	V	V	1,326	96	2.80

Note. w = measurements of water-loaded basement depth; H = measurements of heat flow; k = thermal conductivity ($\text{W m}^{-1}\text{K}^{-1}$); α = thermal expansivity ($\times 10^{-5}\text{K}^{-1}$); C_p = heat capacity (J K^{-1}); T = Mantle temperature ($^{\circ}\text{C}$); z_p = Equilibrium Lithospheric thickness (km); z_r = ridge depth (km) Pac. = Pacific Ocean. Atl. = Atlantic Ocean. V = variable parameters. Bold values denote recovered parameters.

flow constraints. The result highlights the importance of accurate laboratory experiments for k , α and C_p on realistic aggregates of crustal and mantle rocks.

Reference models for cooling and subsidence of oceanic lithosphere have necessarily evolved as observational constraints improve and methodologies become more sophisticated. In Table 2, the databases exploited by key reference models together with values of assumed and recovered parameters are listed. Since the seminal analysis of Parsons and Sclater (1977), it is evident that increasing amounts of subsidence and heat flow measurements have been used to calculate optimal plate cooling models. Figure 8a summarizes the basal temperature estimates and the equilibrium lithospheric thicknesses predicted by the reference models listed in Table 2. Both the HWR-1 and the Stein and Stein (1992) models yield basal temperatures that significantly exceed independent petrologic estimates (Figure 8b). We contend that this discrepancy is a direct consequence of joint inverse modeling where the value of k may be too low. Richards et al. (2018) obtained an equilibrium plate thickness of 136 km with a basal temperature of 1,302°C. We now believe that this plate thickness is likely to be excessively thick, which is the direct consequence of two factors. First, the isostatic sedimentary correction employed by Hoggard et al. (2017) gives rise to a modest overprediction of subsidence for old plate ages. A revised sedimentary correction, which assumes a smaller (i.e., siltier) value of solid grain velocity, has been proposed and implemented by Holdt et al. (2022). This rather minor adjustment slightly decreases the gradient of water-loaded subsidence for plate ages >100 Ma, which in turn yields a thinner equilibrium plate thickness. The adjustment highlights the importance of accurate age-depth measurements. Second, Richards et al. (2018) include “site-specific” heat flow measurements for plate ages of 0–25 Ma. However, many of these measurements are from the Gulf of Aden, where some heat flow measurements may be anomalously elevated due to their proximity to the Afar mantle plume. By fitting these anomalous heat flow values, the optimal plate model must include a steep gradient to match older heat flow measurements, which necessarily yields a much thicker plate. Here, we do not exclusively use “site-specific” measurements between 0 and 25 Ma. Instead, we exploit the global suite of measurements from Hasterok (2013), with their concomitantly greater uncertainty ranges, during this interval (compare Figure 7b with Figure 8b from Richards et al. (2018)). Figure 8 shows that several plate models yield acceptable values of basal temperature. Of these, we equally favor the HWR-2 and HWR-3 models which yield optimal fits to the latest available global databases of age-depth measurements and of revised heat observations. HWR-2 has the advantage of simplicity, while HWR-3 captures known temperature and pressure dependencies of key physical properties, which probably yields a more reliable thermal structure as a function of time.

We emphasize the importance of exploiting a global database of age-depth measurements to obtain a global average plate model. Clearly, this global database masks significant regional anomalies that are generally

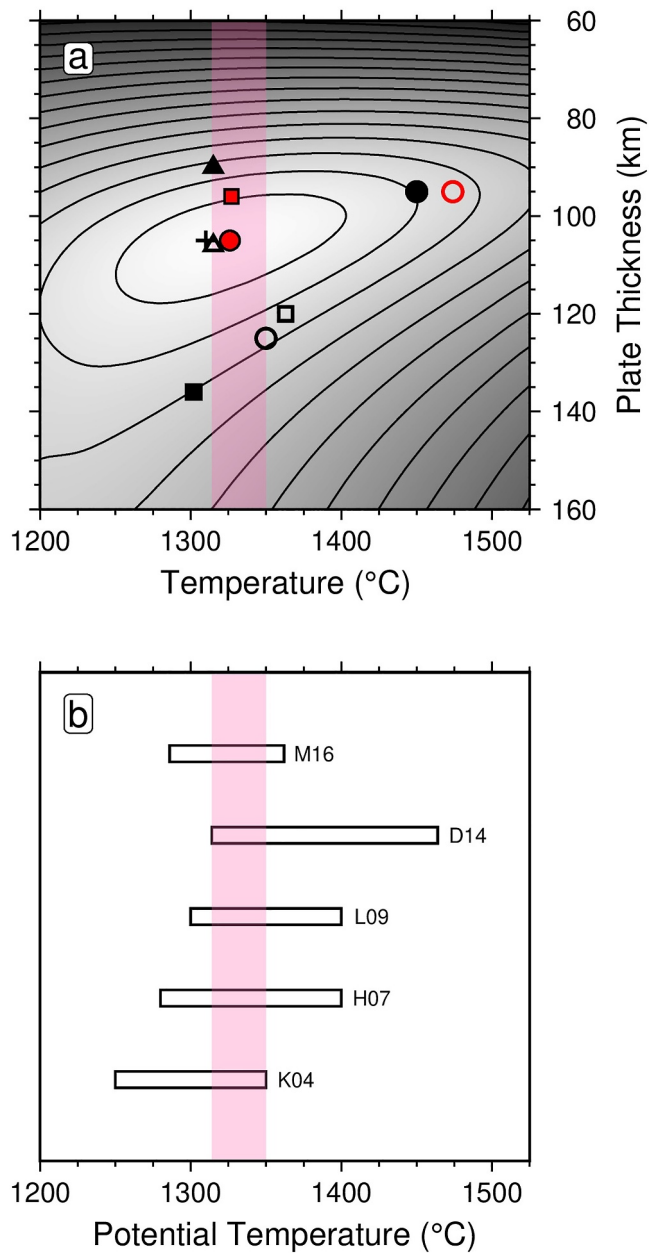


Figure 8. Temperature and plate thickness estimates for range of reference models. (a) Joint misfit between observed and calculated subsidence and heat flow plotted for revised analytical plate model HWR-2 as function of basal temperature and plate thickness (see Figure 5e). Open red circle = HWR-1 model ($T_b = 1,474 \pm 50^\circ\text{C}$; $z_p = 95 \pm 10 \text{ km}$); filled red circle = HWR-2 model ($T_b = 1,326 \pm 50^\circ\text{C}$; $z_p = 105 \pm 10 \text{ km}$); filled red square = HWR-3 model ($T_p = 1,326 \pm 50^\circ\text{C}$; $z_p = 96 \pm 10 \text{ km}$); open black circle = Parsons and Sclater (1977) model ($T_b = 1,350 \pm 275^\circ\text{C}$; $z_p = 125 \pm 10 \text{ km}$); filled black circle = Stein and Stein (1992) model ($T_b = 1,450 \pm 250^\circ\text{C}$; $z_p = 95 \pm 15 \text{ km}$); black cross = CHABLIS model by Doin and Fleitout (1996) ($T_m = 1,310^\circ\text{C}$; $z_p = 105 \text{ km}$); open black square = Hillier and Watts (2005) model ($T_b = 1,363 \pm 7^\circ\text{C}$; $z_p = 120 \pm 21 \text{ km}$); open black triangle = McKenzie et al. (2005) model ($T_p = 1,315 \pm 6^\circ\text{C}$; $z_p = 106 \text{ km}$); filled black triangle = Crosby et al. (2006) model ($T_p = 1,315 \pm 6^\circ\text{C}$, adopted from McKenzie et al. (2005); $z_p = 90 \text{ km}$); filled black square = Richards et al. (2018) ($T_p = 1,302 \pm 50^\circ\text{C}$; $z_p = 136 \pm 30 \text{ km}$); vertical pink band = range which qualitatively honors the overlaps between independent petrologic/geochemical studies shown in panel (b) (i.e., 1,314–1,350°C). (b) Independent estimates of mantle temperature. K04 = 1,250–1,350°C (Katsura et al., 2004); H07 = 1,280–1,400°C (Herzberg et al., 2007); L09 = 1,350 ± 50°C (Lee et al., 2009); D14 = 1,314–1,464°C (Dalton et al., 2014); and M16 = $1318^{+44}_{-32} \text{ }^\circ\text{C}$ (Matthews et al., 2016).

interpreted as mantle dynamic topographic signals. Holdt et al. (2022) mapped the amplitudes and wavelengths of these positive and negative anomalies, which are associated with large-scale and small-scale mantle convective upwellings and downwellings (e.g., Icelandic Plume, Australian-Antarctica Discordance). Notwithstanding these important regional anomalies, it has also been proposed that transient (but global) age-depth shallowing exists. Age-depth measurements from the North Pacific Ocean were used by both Parsons and Sclater (1977) and by Stein and Stein (1992) to constrain their plate cooling models. Building upon these analyses, Crosby et al. (2006) exploited more detailed age-depth measurements from this region to propose that transient shallowing of ~ 250 m occurs for plate ages of 80–130 Ma. This reference model is generated by using an empirical fit to water-loaded age-depth observations. Critically, anomalous observations were removed by excising regions in which substantial long wavelength free-air gravity anomalies correlate with bathymetry. Crosby et al. (2006) also report similar shallowing in four other regions of the oceanic realm. Figure 9c shows that the transient shallowing observed by Crosby et al. (2006) is evident within our database—it is clearly visible when the global subsidence database of Holdt et al. (2022) is sampled within the North Pacific Ocean (Figure 10a). The amplitude and wavelength of the recovered shallowing are almost identical (compare Figures 9a and 9b). Note that the database of Stein and Stein (1992), which includes age-depth measurements from the North Pacific Ocean, also shows transient shallowing between ~ 100 and 130 Ma (see their Figure 1b). Figure 10 shows that the North Pacific Ocean features positive residual depth anomalies in the vicinity of various hotspot tracks within this 80–130 Ma window. In addition, the observed shallowing of age-depth measurements in this region becomes emergent because only one flank of the cooling plate has been sampled (Figure 10b). Several other regions were also used by Crosby et al. (2006) to demonstrate transient shallowing. However, these smaller regions tend to feature the same age-depth sampling pathology. Figure 10c shows that these regions also feature mantle plumes within the 80 and 130 Ma age window: the Bermuda swell of the Northwest Atlantic Ocean; the Cape Verde, Madeira and New England swells of the Northeast Atlantic Ocean; and the Angolan and Vema swells of the Southwest Atlantic Ocean. Figure 10c also shows that these regions do not include significant downwellings which lie within the 80–130 Ma window (e.g., Argentine Abyssal Plain, Weddell Sea, Bay of Bengal). Figure 2b demonstrates that transient shallowing is not evident on a global scale, presumably because positive and negative regional anomalies are averaged out on a global scale.

The overall flattening of global age-depth measurements to a water-loaded depth of 6 km from approximately 80 Ma is matched by a flattening of heat flow measurements, which tend toward 0.05 W m^{-2} at old plate ages. Parsons and McKenzie (1978) suggest that the oceanic lithosphere consists of mechanical and thermal boundary layers. As the plate cools, both of these layers thicken with age. From a fluid dynamical perspective, the thermal boundary layer should become unstable and convectively overturn for plate ages that exceed about 60 Ma. A convective instability is invoked by Parsons and McKenzie (1978) in order to stabilize lithospheric thickness. We suggest that instabilities occur on smaller length scales and therefore on shorter timescales than hitherto expected, such that they cryptically lie within the scatter produced by residual depth anomalies.

We end this contribution by addressing the rheological structure of cooling oceanic lithosphere. Figures 11a and 11b show the evolving thermal structure of oceanic lithosphere calculated for the HWR-2 and HWR-3 models, respectively. In both cases, the distribution of intraplate and outer rise earthquakes analyzed by Craig et al. (2014) occur at temperatures of $< 700^\circ\text{C}$, in broad agreement with some, but not all, previous studies (Craig et al., 2014; McKenzie et al., 2005; Richards et al., 2018). This revised estimate is now consistent with laboratory creep experiments carried out upon dry polycrystalline olivine aggregates (Boettcher et al., 2007; Goetze & Evans, 1979). At greater depths, our recovered temperature structure can be compared with the surface wave dispersion results of Burgos et al. (2014). They suggest that the lithosphere-asthenosphere boundary layer can be identified using a combination of two proxies—vertically polarized shear wave velocity measurements, V_{sv} , and orientations of the fast axis of azimuthal anisotropy, ψ_G . For oceanic lithosphere older than ~ 60 Ma, the top of the lithosphere-asthenosphere boundary layer identified by measurements of ψ_G broadly coincides with a predicted temperature of about $1,300^\circ\text{C}$ or falls just beneath the base of the plate (Figures 11a and 11b). Note that ψ_G measurements exhibit a flattening with age from 80 Ma of both the upper and lower bounds of the measured cloud. This observation is broadly consistent with age-depth and heat flow measurements.

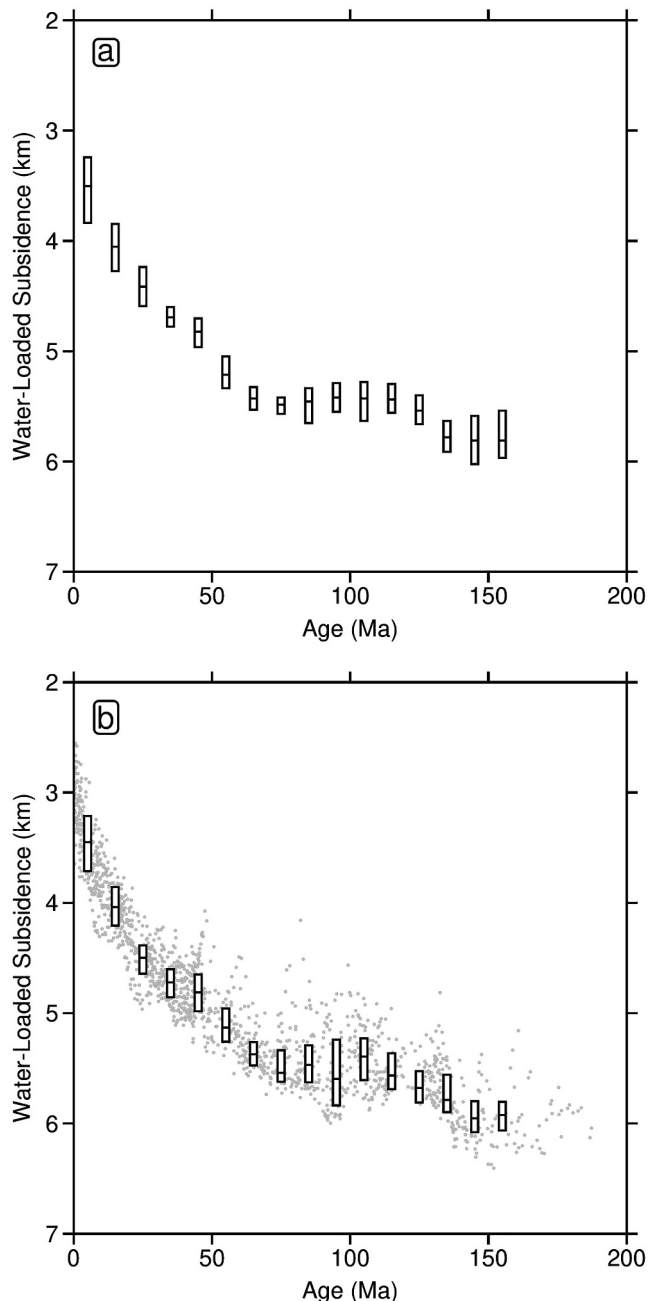


Figure 9. Analysis of Crosby et al. (2006) observations. (a) Age-depth measurements as function of oceanic plate age from portion of Pacific Ocean analyzed by Crosby et al. (2006). Horizontal bars with vertical gray boxes = median values with interquartile ranges of age-depth measurements binned every 10 Ma. Note plate shallowing centered on 100 Ma. (b) Age-depth measurements as function of oceanic plate age extracted from revised and augmented database of Holdt et al. (2022). Gray points = age-depth measurements from same portion of Pacific Ocean (see Pacific box of Figure 10 for location). Note that age-depth measurements are excluded in regions with anomalous topography and gravity, as identified by Crosby et al. (2006). Horizontal bars with vertical gray boxes = median values with interquartile ranges of age-depth measurements binned every 10 Ma. Note recovery of plate shallowing centered on 100 Ma.

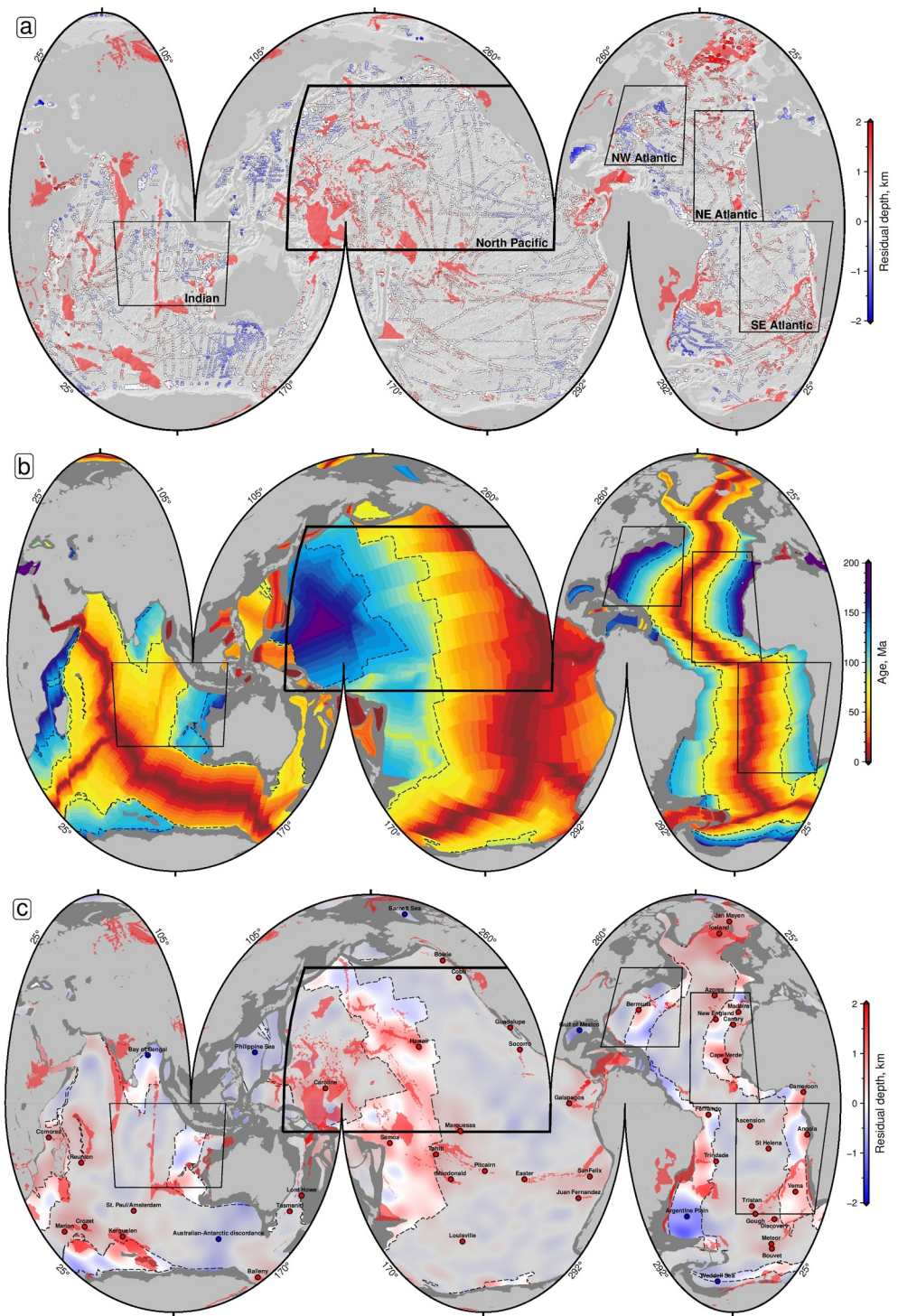


Figure 10. Regions selected in plate model study of Crosby et al. (2006). (a) Global distribution of residual depth measurements averaged over 1° bins. Circles = measurements with both sedimentary and crustal corrections; triangles = measurements for which only sedimentary corrections are applied. Red polygons = large igneous provinces and seamounts Coffin et al. (2006). Black box with thick outline = region of Pacific Ocean used to generate reference model by Crosby et al. (2006). Black boxes with thin outline = other regions where transient shallowing is observed by Crosby et al. (2006). (b) Augmented and revised age grid of Seton et al. (2020). Dashed contours = 80 and 130 Ma isochrons. (c) Spherical harmonic representation of residual depth measurements where $l_{\max} = 40$. Transparent gray fill = oceanic crust < 80 Ma and > 130 Ma (i.e., region without transient shallowing observed by Crosby et al. (2006)). Red/blue circles = mantle plumes/drawdowns (see Table S1).

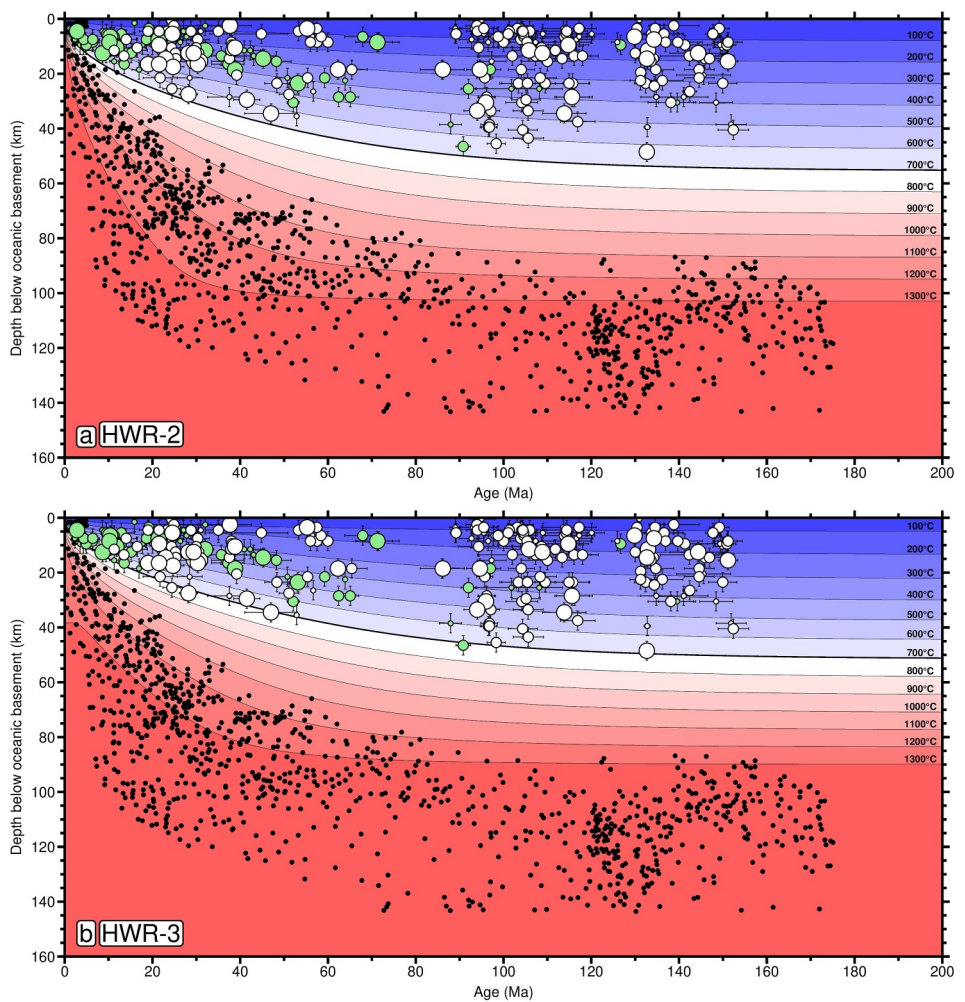


Figure 11. Thermal structure of oceanic lithosphere. (a) Thermal structure of oceanic lithosphere calculated using HWR-2 model. Contour lines = isothermal surfaces; green/white circles with errors = oceanic intraplate/outer rise earthquakes taken from Craig et al. (2014) where small, medium and large circles = $M_b < 5.5$, $5.5\text{--}6.5$, and >6.5 ; bold contour line = 700°C isothermal surface, which identifies temperature above which oceanic earthquakes occur; solid black circles = measurements of depth to lithosphere-asthenosphere boundary zone determined from the orientation of azimuthal anisotropy, ψ_G (Burgos et al., 2014). (b) Same for HWR-3 model.

7. Conclusions

In this study, a global database of accurate age-depth measurements is combined with an existing database of filtered heat flow measurements to revisit the well-known plate cooling model. Our primary goal is to identify the simplest plate model that yields the smallest misfit between combined age-depth and heat flow measurements. In order to accomplish this task, we have explored a variety of analytical and numerical plate models which respectively assume that thermal conductivity, thermal expansivity and specific heat capacity are constant or vary as a function of temperature and pressure using experimental constraints. The optimal analytical model yields a basal temperature of $1,326 \pm 50^\circ\text{C}$ and an equilibrium plate thickness of 105 ± 10 km for a zero-age depth of 2.50 ± 0.3 km. This value of basal temperature is consistent with independent constraints. A more physically accurate numerical model fits subsidence and heat flow observations equally well and yields almost identical values of basal temperature and equilibrium plate thickness. Spatial analysis of our global database of age-depth measurements shows that previously described transient shallowing for plate ages of 80–130 Ma is a product of geographic sampling. This lack of shallowing suggests that convective instabilities, which are thought to maintain constant plate thickness, probably act on shorter timescales and smaller length scales. Finally, our revised plate model can be used to calculate the thermal structure of the lithosphere as a function of time, to estimate that the

maximum depth of intraplate earthquakes is bound by the 700°C isothermal surface, and to accurately estimate residual depth anomalies which represent maximum observable mantle dynamic topography.

Data Availability Statement

Data files, code, and final models are available at Holdt et al. (2025). Residual depth measurements are published by Holdt et al. (2022), heat flow measurements are published by Hasterok et al. (2011), the age grid is published by Seton et al. (2020), earthquake depths are published by Craig et al. (2014) and azimuthal anisotropy measurements are published by Burgos et al. (2014).

Acknowledgments

MCH was supported by the Gates Cambridge Trust and by Project InnerSpace. We are grateful for G. Burgos and J.-P. Montagner for sending us their global azimuthal anisotropic measurements. We also thank H. Doran, A. Jackson and D. Lyness for their help. Department of Earth Sciences contribution number esc.120430.

References

- Afonso, J. C., Ranalli, G., & Fernández, M. (2007). Density structure and buoyancy of the oceanic lithosphere revisited. *Geophysical Research Letters*, 34(10), 2–6. <https://doi.org/10.1029/2007GL029515>
- Berman, R. G., & Aranovich, L. Y. (1997). Optimized standard state and solution properties of minerals I. Model calibration for olivine, orthopyroxene, cordierite, garnet, and ilmenite in the system FeO-MgO-CaO-Al₂O₃-TiO₂-SiO₂. *Contributions to Mineralogy and Petrology*, 126(1–2), 1–24. <https://doi.org/10.1007/s004100050232>
- Boettcher, M. S., McGarr, A., Johnston, M., Jordan, T. H., Heesakkers, V., & Reches, Z. (2007). Constraints on seismogenesis of small earthquakes ($-2.8 \leq M \leq 3$) defined by the dense instrument network of the natural earthquake laboratory in South African Mines (NELSAM). In *Agu fall meeting abstracts* (Vol. 2007), p. S33D-02.
- Bouhifd, M. A., Andrault, D., Fiquet, G., & Richet, P. (1996). Thermal expansion of forsterite up to the melting point. *Geophysical Research Letters*, 23(10), 1143–1146. <https://doi.org/10.1029/96GL01118>
- Burgos, G., Montagner, J. P., Beucler, E., Capdeville, Y., Mocquet, A., & Drilleau, M. (2014). Oceanic lithosphere-asthenosphere boundary from surface wave dispersion data. *Journal of Geophysical Research: Solid Earth*, 119(2), 1079–1093. <https://doi.org/10.1002/2013JB010528>
- Carlson, R. L., & Jay Miller, D. (2004). Influence of pressure and mineralogy on seismic velocities in oceanic gabbros: Implications for the composition and state of the lower oceanic crust. *Journal of Geophysical Research*, 109(B9), 28. <https://doi.org/10.1029/2003JB002699>
- Carlsaw, H. S., & Jaeger, J. C. (1959). *Conduction of heat in solids* (2nd ed.). Oxford University Press.
- Christeson, G. L., Goff, J. A., & Reece, R. S. (2019). Synthesis of oceanic crustal structure from two-dimensional seismic profiles. *Reviews of Geophysics*, 57(2), 504–529. <https://doi.org/10.1029/2019RG000641>
- Coffin, M. F., Duncan, R. A., Eldholm, O., Fitton, J. G., Frey, F. A., Larsen, H. C., et al. (2006). Large igneous provinces and scientific ocean drilling: Status quo and a look ahead. *Oceanography*, 19(4), 150–160. <https://doi.org/10.5670/oceanog.2006.13>
- Coffin, M. F., & Eldholm, O. (1994). Large igneous provinces: Crustal structure, dimensions, and external consequences. *Reviews of Geophysics*, 32(1), 1–36. <https://doi.org/10.1029/93RG02508>
- Craig, T. J., Copley, A., & Jackson, J. (2014). A reassessment of outer-rise seismicity and its implications for the mechanics of oceanic lithosphere. *Geophysical Journal International*, 197(1), 63–89. <https://doi.org/10.1093/gji/ggu013>
- Crosby, A. G., & McKenzie, D. P. (2009). An analysis of young ocean depth, gravity and global residual topography. *Geophysical Journal International*, 178(3), 1198–1219. <https://doi.org/10.1111/j.1365-246X.2009.04224.x>
- Crosby, A. G., McKenzie, D. P., & Slater, J. G. (2006). The relationship between depth, age and gravity in the oceans. *Geophysical Journal International*, 166(2), 553–573. <https://doi.org/10.1111/j.1365-246X.2006.03015.x>
- Dalton, C. A., Langmuir, C. H., & Gale, A. (2014). Geophysical and geochemical evidence for deep temperature variations beneath mid-ocean ridges. *Science*, 344(6179), 80–83. <https://doi.org/10.1126/science.1249466>
- Davies, G. F. (1988). Ocean bathymetry and mantle convection. 2. Small-Scale Flow. *Journal of Geophysical Research*, 93(B9), 10481–10488. <https://doi.org/10.1029/jb093ib09p10467>
- Davis, E. E., & Lister, C. R. (1974). Fundamentals of ridge crest topography. *Earth and Planetary Science Letters*, 21(4), 405–413. [https://doi.org/10.1016/0012-821X\(74\)90180-0](https://doi.org/10.1016/0012-821X(74)90180-0)
- Dick, H. J. B., Natland, J. H., Alt, J. C., Bach, W., Bideau, D., Gee, J. S., et al. (2000). A long in situ section of the lower ocean crust: Results of ODP Leg 176 drilling at the Southwest Indian ridge. *Earth and Planetary Science Letters*, 179(1), 31–51. [https://doi.org/10.1016/S0012-821X\(00\)00102-3](https://doi.org/10.1016/S0012-821X(00)00102-3)
- Doin, M. P., & Fleitout, L. (1996). Thermal evolution of the oceanic lithosphere: An alternative view. *Earth and Planetary Science Letters*, 142(1–2), 121–136. [https://doi.org/10.1016/0012-821x\(96\)00082-9](https://doi.org/10.1016/0012-821x(96)00082-9)
- Galloway, W. E., Whiteaker, T. L., & Ganey-Curry, P. (2011). History of Cenozoic North American drainage basin evolution, sediment yield, and accumulation in the Gulf of Mexico basin. *Geosphere*, 7(4), 938–973. <https://doi.org/10.1130/GES00647.1>
- Goetze, C., & Evans, B. (1979). Stress and temperature in the bending lithosphere as constrained by experimental rock mechanics. *Geophysical Journal International*, 59(3), 463–478. <https://doi.org/10.1111/j.1365-246X.1979.tb02567.x>
- Goranson, R. W. (1942). Heat capacity; Heat of fusion. In J. Birch, F. Schairer, & H. Spicer (Eds.), *Handbook of physical constraints* (Vol. 36, pp. 223–242). Geological Society of America, Special Paper. <https://doi.org/10.1130/SPE36-p223>
- Goutorbe, B., & Hillier, J. K. (2013). An integration to optimally constrain the thermal structure of oceanic lithosphere. *Journal of Geophysical Research: Solid Earth*, 118(1), 432–446. <https://doi.org/10.1029/2012JB009527>
- Grose, C. J., & Afonso, J. C. (2013). Comprehensive plate models for the thermal evolution of oceanic lithosphere. *Geochemistry, Geophysics, Geosystems*, 14(9), 3751–3778. <https://doi.org/10.1029/ggge.2023>
- Hasterok, D. (2013). Global patterns and vigor of ventilated hydrothermal circulation through young seafloor. *Earth and Planetary Science Letters*, 380, 12–20. <https://doi.org/10.1016/j.epsl.2013.08.016>
- Hasterok, D., Chapman, D. S., & Davis, E. E. (2011). Oceanic heat flow: Implications for global heat loss. *Earth and Planetary Science Letters*, 311(3–4), 386–395. <https://doi.org/10.1016/j.epsl.2011.09.044>
- Herzberg, C., Asimow, P. D., Arndt, N., Niu, Y., Lesher, C. M., Fitton, J. G., et al. (2007). Temperatures in ambient mantle and plumes: Constraints from basalts, picrites, and komatiites. *Geochemistry, Geophysics, Geosystems*, 8(2), Q02006. <https://doi.org/10.1029/2006GC001390>
- Hilde, T. W. C., Isezaki, N., & Wageman, J. M. (1976). Mesozoic Sea-floor spreading in the North Pacific. *The geophysics of the Pacific Ocean basin and its margin*, 19, 205–226. <https://doi.org/10.1029/gm019p0205>

- Hillier, J. K., & Watts, A. B. (2005). Relationship between depth and age in the North Pacific ocean. *Journal of Geophysical Research*, 110(2), 1–22. <https://doi.org/10.1029/2004JB003406>
- Hofmeister, A. M. (1999). Mantle values of thermal conductivity and the geotherm from phonon lifetimes. *Science*, 283(5408), 1699–1706. <https://doi.org/10.1126/science.283.5408.1699>
- Hofmeister, A. M. (2005). Dependence of diffusive radiative transfer on grain-size, temperature, and Fe-content: Implications for mantle processes. *Journal of Geodynamics*, 40(1), 51–72. <https://doi.org/10.1016/j.jog.2005.06.001>
- Hofmeister, A. M. (2007). Pressure dependence of thermal transport properties. *Proceedings of the National Academy of Sciences of the United States of America*, 104(22), 9192–9197. <https://doi.org/10.1073/pnas.0610734104>
- Hofmeister, A. M. (2010). Thermal diffusivity of oxide perovskite compounds at elevated temperature. *Journal of Applied Physics*, 107(10), 537–549. <https://doi.org/10.1063/1.3371815>
- Hoggard, M. J., White, N., & Al-Attar, D. (2016). Global dynamic topography observations reveal limited influence of large-scale mantle flow. *Nature Geoscience*, 9(6), 456–463. <https://doi.org/10.1038/ngeo2709>
- Hoggard, M. J., Winterbourne, J., Czarnota, K., & White, N. (2017). Oceanic residual depth measurements, the plate cooling model, and global dynamic topography. *Journal of Geophysical Research: Solid Earth*, 122(3), 2328–2372. <https://doi.org/10.1002/2016JB013457>
- Holdt, M. C., White, N., & Richards, F. (2025). Supplementary material: “a revised oceanic plate cooling model” [Dataset]. Zenodo. <https://doi.org/10.5281/zenodo.14691107>
- Holdt, M. C., White, N. J., Stephenson, S. N., & Conway-Jones, B. W. (2022). Densely sampled global dynamic topographic observations and their significance. *Journal of Geophysical Research: Solid Earth*, 127(7), e2022JB024391. <https://doi.org/10.1029/2022JB024391>
- Huang, J., & Zhong, S. (2005). Sublithospheric small-scale convection and its implications for the residual topography at old ocean basins and the plate model. *Journal of Geophysical Research*, 110(5), 1–17. <https://doi.org/10.1029/2004JB003153>
- Katsura, T., Yamada, H., Nishikawa, O., Song, M., Kubo, A., Shinmei, T., et al. (2004). Olivine-wadsleyite transition in the system (Mg,Fe)₂SiO₄. *Journal of Geophysical Research*, 109(B02), B02209. <https://doi.org/10.1029/2003jb002438>
- Kelemen, P. B., Kikawa, E., Miller, D. J., & Party, S. S. (2004). Shipboard Scientific party, Leg 209 summary; Technical Report (Vol. 209).
- Knapp, J. H., Knapp, C. C. D., Connor, J. A., McBride, J. H., & Simmons, M. D. (2007). Deep seismic exploration of the South Caspian Basin: Lithosphere-scale imaging of the world’s deepest basin. In P. O. Yilmaz & G. H. Isaksen (Eds.), *Oil and gas of the greater caspian area* (pp. 47–49). AAPG Special Volumes. <https://doi.org/10.1306/1205831St553248>
- Korenaga, J. (2015). Seafloor topography and the thermal budget of Earth. *Geological Society of America Special Paper*, 514, 167–185. [https://doi.org/10.1130/2015.2514\(11\)](https://doi.org/10.1130/2015.2514(11))
- Korenaga, T., & Korenaga, J. (2016). Evolution of young oceanic lithosphere and the meaning of seafloor subsidence rate. *Journal of Geophysical Research: Solid Earth*, 121(9), 6315–6332. <https://doi.org/10.1002/2016JB013395>
- Korenaga, T., Korenaga, J., Kawakatsu, H., & Yamano, M. (2021). A new reference model for the evolution of oceanic lithosphere in a cooling Earth. *Journal of Geophysical Research: Solid Earth*, 126(6), 1–29. <https://doi.org/10.1029/2020JB021528>
- Larson, R. L., & Hilde, T. W. (1975). A revised time scale of magnetic reversals for the Early Cretaceous and Late Jurassic. *Journal of Geophysical Research*, 80(17), 2586–2594. <https://doi.org/10.1029/JB080i017p02586>
- Lee, C. T. A., Luffi, P., Plank, T., Dalton, H., & Leeman, W. P. (2009). Constraints on the depths and temperatures of basaltic magma generation on Earth and other terrestrial planets using new thermobarometers for mafic magmas. *Earth and Planetary Science Letters*, 279(1–2), 20–33. <https://doi.org/10.1016/j.epsl.2008.12.020>
- Matthews, S., Shorttle, O., & MacLennan, J. (2016). The temperature of the Icelandic mantle from olivine-spinel aluminum exchange thermometry. *Geochemistry, Geophysics, Geosystems*, 17(11), 4725–4752. <https://doi.org/10.1002/2016GC006497>
- McKenzie, D. P. (1967). Some remarks on heat flow and gravity anomalies. *Journal of Geophysical Research*, 72(24), 6261–6273. <https://doi.org/10.1029/jz072i024p06261>
- McKenzie, D. P., & Bickle, M. J. (1988). The volume and composition of melt generated by extension of the lithosphere. *Journal of Petrology*, 29(3), 625–679. <https://doi.org/10.1093/petrology/29.3.625>
- McKenzie, D. P., Jackson, J. A., & Priestley, K. (2005). Thermal structure of oceanic and continental lithosphere. *Earth and Planetary Science Letters*, 233(3–4), 337–349. <https://doi.org/10.1016/j.epsl.2005.02.005>
- Menard, H. W. (1973). Depth anomalies and the bobbing motion of drifting islands. *Journal of Geophysical Research*, 78(23), 5128–5137. <https://doi.org/10.1029/jb078i023p05128>
- Parsons, B., & McKenzie, D. P. (1978). Mantle convection and the thermal structure of the plates. *Journal of Geophysical Research*, 83(B9), 4485–4496. <https://doi.org/10.1029/JB083iB09p04485>
- Parsons, B., & Sclater, J. G. (1977). An analysis of the variation of ocean floor bathymetry and heat flow with age. *Journal of Geophysical Research*, 82(5), 803–827. <https://doi.org/10.1029/jb082i005p00803>
- Pertermann, M., & Hofmeister, A. M. (2006). Thermal diffusivity of olivine-group minerals at high temperature. *American Mineralogist*, 91(11–12), 1747–1760. <https://doi.org/10.2138/am.2006.2105>
- Priestley, K., Ho, T., Takei, Y., & McKenzie, D. P. (2024). The thermal and anisotropic structure of the top 300 km of the mantle. *Earth and Planetary Science Letters*, 626, 118525. <https://doi.org/10.1016/j.epsl.2023.118525>
- Priestley, K., & McKenzie, D. P. (2006). The thermal structure of the lithosphere from shear wave velocities. *Earth and Planetary Science Letters*, 244(1–2), 285–301. <https://doi.org/10.1016/j.epsl.2006.01.008>
- Priestley, K., & McKenzie, D. P. (2013). The relationship between shear wave velocity, temperature, attenuation and viscosity in the shallow part of the mantle. *Earth and Planetary Science Letters*, 381, 78–91. <https://doi.org/10.1016/j.epsl.2013.08.022>
- Richards, F. D., Hoggard, M., Crosby, A., Ghelichkhan, S., & White, N. (2020). Structure and dynamics of the oceanic lithosphere–asthenosphere system. *Physics of the Earth and Planetary Interiors*, 309(July), 106559. <https://doi.org/10.1016/j.pepi.2020.106559>
- Richards, F. D., Hoggard, M. J., Cowton, L. R., & White, N. J. (2018). Reassessing the thermal structure of oceanic lithosphere with revised global Inventories of basement depths and heat flow measurements. *Journal of Geophysical Research: Solid Earth*, 123(10), 9136–9161. <https://doi.org/10.1029/2018JB015998>
- Rowley, D. B. (2019). Oceanic axial depth and age-depth distribution of oceanic lithosphere: Comparison of magnetic anomaly picks versus age-grid models. *Lithosphere*, 11(1), 21–43. <https://doi.org/10.1130/L1027.1>
- Schatz, J. F., & Simmons, G. (1972). Thermal conductivity of Earth materials at high temperatures. *Journal of Geophysical Research*, 77(35), 6966–6983. <https://doi.org/10.1029/jb077i035p06966>
- Sclater, J., Hasterok, D., Goutorbe, B., Hillier, J. K., & Negrete, R. (2014). Encyclopedia of marine Geosciences. *Encyclopedia of Marine Geosciences*, 1–16. <https://doi.org/10.1007/978-94-007-6644-0>
- Seton, M., Müller, R. D., Zahirovic, S., Williams, S., Wright, N. M., Cannon, J., et al. (2020). A global data set of present-day oceanic crustal age and seafloor spreading parameters. *Geochemistry, Geophysics, Geosystems*, 21(10), 1–15. <https://doi.org/10.1029/2020GC009214>

- Stein, C., & Stein, S. (1992). A model for the global variation in oceanic depth and heat flow with lithospheric age. *Nature*, 359(10), 123–129. <https://doi.org/10.1038/359123a0>
- Steinberger, B., & Becker, T. W. (2018). A comparison of lithospheric thickness models. *Tectonophysics*, 746, 325–338. <https://doi.org/10.1016/j.tecto.2016.08.001>
- Straume, E. O., Gaina, C., Medvedev, S., Hochmuth, K., Gohl, K., Whittaker, J. M., et al. (2019). GlobSed: Updated total sediment thickness in the world's oceans. *Geochemistry, Geophysics, Geosystems*, 20(4), 1756–1772. <https://doi.org/10.1029/2018GC008115>
- Sydorenko, G., Stephenson, R., Yegorova, T., Starostenko, V., Tolkunov, A., Janik, T., et al. (2017). Geological structure of the northern part of the Eastern Black Sea from regional seismic reflection data including the DOBRE-2 CDP profile. In M. Sosson, R. Stephenson, & S. Adamia (Eds.), *Tectonic evolution of the eastern black sea and caucasus* (Vol. 428, pp. 307–321). Geological Society of London. <https://doi.org/10.1144/SP428.15>
- Takeuchi, H., & Sakata, S. (1970). Convection in a mantle with variable viscosity. *Journal of Geophysical Research*, 75(5), 921–927. <https://doi.org/10.1029/jb075i005p00921>
- Turcotte, D. L., & Oxburgh, E. R. (1967). Finite amplitude convective cells and continental drift. *Journal of Fluid Mechanics*, 28(1), 29–42. <https://doi.org/10.1017/S0022112067001880>
- VanTongeren, J. A., Kelemen, P. B., Garrido, C. J., Godard, M., Hanghoj, K., Braun, M., & Pearce, J. A. (2021). The composition of the lower oceanic crust in the Wadi Khafifah section of the southern Samail (Oman) ophiolite. *Journal of Geophysical Research: Solid Earth*, 126(11), e2021JB021986. <https://doi.org/10.1029/2021JB021986>
- Vogt, P. R., Anderson, C. N., & Bracey, D. R. (1971). Mesozoic magnetic anomalies, sea-floor spreading, and geomagnetic reversals in the southwestern North Atlantic. *Journal of Geophysical Research*, 76(20), 4796–4823. <https://doi.org/10.1029/jb076i020p04796>
- Von Herzen, R. P., & Uyeda, S. (1963). Heat flow through the eastern Pacific Ocean floor. *Journal of Geophysical Research*, 68(14), 4219–4250. <https://doi.org/10.1029/JZ068i014p04219>
- Wessel, P., Sandwell, D. T., & Kim, S. S. (2010). The global seamount census. *Oceanography*, 23(1), 24–33. <https://doi.org/10.5670/oceanog.2010.60>

References From the Supporting Information

- Benoit, M. H., Long, M. D., & King, S. D. (2013). Anomalously thin transition zone and apparently isotropic upper mantle beneath Bermuda: Evidence for upwelling. *Geochemistry, Geophysics, Geosystems*, 14(10), 4282–4291. <https://doi.org/10.1002/ggge.20277>
- Celli, N. L., Lebedev, S., Schaeffer, A. J., Ravenna, M., & Gaina, C. (2020). The upper mantle beneath the South Atlantic Ocean, South America and Africa from waveform tomography with massive data sets. *Geophysical Journal International*, 221(1), 178–204. <https://doi.org/10.1093/gji/ggz574>
- Courtillot, V., Davaille, A., Besse, J., & Stock, J. (2003). Three distinct types of hotspots in the Earth's mantle. *Earth and Planetary Science Letters*, 205(3–4), 295–308. [https://doi.org/10.1016/S0012-821X\(02\)01048-8](https://doi.org/10.1016/S0012-821X(02)01048-8)
- Johnson, K. T., Graham, D. W., Rubin, K. H., Nicolaysen, K., Scheirer, D. S., Forsyth, D. W., et al. (2000). Boomerang seamount: The active expression of the Amsterdam-St. Paul hotspot, Southeast India ridge. *Earth and Planetary Science Letters*, 183(1–2), 245–259. [https://doi.org/10.1016/S0012-821X\(00\)00279-X](https://doi.org/10.1016/S0012-821X(00)00279-X)
- Klöcking, M., Hoggard, M. J., Rodríguez Tribaldos, V., Richards, F. D., Guimarães, A. R., MacLennan, J., & White, N. J. (2020). A tale of two domes: Neogene to recent volcanism and dynamic uplift of northeast Brazil and southwest Africa. *Earth and Planetary Science Letters*, 547, 116464. <https://doi.org/10.1016/j.epsl.2020.116464>
- Liu, X., & Zhao, D. (2014). Seismic evidence for a mantle plume beneath the Cape Verde hotspot. *International Geology Review*, 56(10), 1213–1225. <https://doi.org/10.1080/00206814.2014.930720>
- Maund, J. G., Rex, D. C., Le Roex, A. P., & Reid, D. L. (1988). Volcanism on Gough Island: A revised stratigraphy. *Geological Magazine*, 125(2), 175–181. <https://doi.org/10.1017/S0016756800009572>
- Miller, M. S., O'Driscoll, L. J., Butcher, A. J., & Thomas, C. (2015). Imaging Canary Island hotspot material beneath the lithosphere of Morocco and southern Spain. *Earth and Planetary Science Letters*, 431, 186–194. <https://doi.org/10.1016/j.epsl.2015.09.026>
- Niu, F., Solomon, S. C., Silver, P. G., Suetsugu, D., & Inoue, H. (2002). Mantle transition-zone structure beneath the South Pacific Superswell and evidence for a mantle plume underlying the society hotspot. *Earth and Planetary Science Letters*, 198(3–4), 371–380. [https://doi.org/10.1016/S0012-821X\(02\)00523-X](https://doi.org/10.1016/S0012-821X(02)00523-X)
- Obayashi, M., Yoshimitsu, J., Suetsugu, D., Shiobara, H., Sugioka, H., Ito, A., et al. (2021). Interrelation of the stagnant slab, Ontong Java Plateau, and intraplate volcanism as inferred from seismic tomography. *Scientific Reports*, 11(1), 1–10. <https://doi.org/10.1038/s41598-021-99833-5>